Archival Diagnostics for Potential Background Contaminants of Project Hephaistos Dyson Sphere Candidates

T. Ren,[1★] M. A. Garrett,[1,2,7], E. Zackrisson,[3], A. J. Korn,[3] A. P. V. Siemion,[1,4,5,6,7] J. T. Wright,[8,9,10] and A. Brandeker[11]

[1] *Jodrell Bank Centre for Astrophysics, Department of Physics and Astronomy, University of Manchester, Oxford Road, Manchester M13 9PL, UK*
[2] *Leiden Observatory, Leiden University, PO Box 9513, NL-2300 RA Leiden, the Netherlands*
[3] *Observational Astrophysics, Department of Physics and Astronomy, Uppsala University, Box 516, SE-751 20 Uppsala, Sweden*
[4] *Breakthrough Listen, Astrophysics sub-department, Department of Physics, University of Oxford, Denys Wilkinson Building, Keble Road, Oxford OX1 3RH, UK*
[5] *Berkeley SETI Research Center, University of California, Berkeley, CA 94720, USA*
[6] *SETI Institute, 339 Bernardo Avenue, Suite 200, Mountain View, CA 94043, USA*
[7] *University of Malta, Institute of Space Sciences and Astronomy, Msida, MSD2080, Malta*
[8] *Department of Astronomy and Astrophysics, The Pennsylvania State University, University Park, PA 16802, USA*
[9] *Penn State Extraterrestrial Intelligence Center, The Pennsylvania State University, University Park, PA 16802, USA*
[10] *Center for Exoplanets and Habitable Worlds, The Pennsylvania State University, University Park, PA 16802, USA*
[11] *Department of Astronomy, Stockholm University, AlbaNova University Center, 10691 Stockholm, Sweden*

arXiv:2607.03619v2 [astro-ph.SR] 4 Aug 2026

Submitted to the Monthly Notices of the Royal Astronomical Society (MNRAS).

ABSTRACT

We report on the diagnostic investigation of nine Project Hephaistos Dyson Sphere candidate M-dwarfs based on archival data. By comparing the *Gaia* DR3 positions with epoch 2016.0, propagated to the *AllWISE* epoch, with the mid-infrared centroids measured from the *AllWISE* images, together with deep archival optical/near-infrared imaging, we identified significant background contamination in candidates B and C—candidate B coincident with a radio counterpart showing a power-law-like spectrum with a radio spectral index $\alpha = 0.63 \pm 0.11$, and candidate C with a near-infrared companion at a 3.75″ offset. Candidate A provides suggestive evidence through a radio counterpart with $\alpha = 0.40 \pm 0.35$, while candidates E, F, H and J show some marginal evidence. These systems exhibit either significant astrometric offsets or visible interlopers, indicating that the mid-infrared excess likely arises from line-of-sight contamination by hot, dust-obscured galaxies. However, candidates D and I still lack obvious signs of contamination. Dedicated observations are therefore essential to characterise these potential interlopers, in order to eliminate false positives and ensure that techno-signature searches focus on the most robust Dyson Sphere candidates.

Key words: extraterrestrial intelligence – infrared: stars – infrared: galaxies

1 INTRODUCTION

In mid-2024, Project Hephaistos[1] reported seven Dyson sphere candidates. Dyson spheres are hypothetical megastructures envisioned to harvest stellar energy, with their most distinctive observable signature being excess infrared emission produced by the re-radiation of absorbed starlight as thermal waste heat (Dyson 1960; Wright 2020). The project identified these candidates by identifying stars with significant mid-infrared (MIR) excess from a sample of approximately 5 million stars detected by *Gaia*, 2MASS, and WISE, all within 300 parsecs of us (Suazo et al. 2024). All candidates are M-dwarf stars exhibiting MIR excess in the WISE W3 and W4 bands, with spectral energy distributions (SEDs) consistent with blackbody temperatures in the range of 100–300 K, as expected from partial Dyson Sphere models (Suazo et al. 2022).

Just as radio SETI surveys targeting nearby stars frequently encompass background extragalactic objects within the telescope's field of view (Garrett & Siemion 2023), this same principle applies analogously to infrared SETI searches. The cross-matching of seven candidates with archival radio surveys revealed offset radio counterparts for candidates A, B, and G (Ren, Garrett & Siemion 2024). High-resolution e-MERLIN (1.5 GHz) and EVN (5 GHz) observations (Ren, Garrett & Siemion 2025) confirmed that J2335−0004, the radio source associated with candidate G, is a high brightness temperature ($> 1 \times 10^8$ K) background active galactic nucleus (AGN) located more than 5 arcseconds from the propagated epoch 2024.4 *Gaia* position of the star. We did not detect radio emission exceeding 3σ at the stellar coordinates at 1.5 or 5 GHz, and thus found no evidence of broadband radio emission at these frequencies that could represent unintentional radio leakage from the candidate system.

Furthermore, the positional offset analysis of the *ALLWISE* images revealed that while the emission in the WISE W1 and W2 bands is associated with the M-dwarf, the W3 and W4 emission is primarily contributed by the offset AGN. The spectral energy distribution (SED) of the AGN suggested that it was most likely a Hot Dust-

★ E-mail: tongtian.ren@manchester.ac.uk (TR)
[1] https://www.astro.uu.se/~ez/hephaistos/hephaistos.html

© 2026 The Authors

Obscured Galaxy (Hot DOG; Assef et al. 2015; Tsai et al. 2015) - bright in W3 and W4 bands but faint and obscured in the W1 and W2 bands.

Hot Dust-Obscured Galaxies (Hot DOGs) are a rare class of luminous galaxies powered by heavily obscured supermassive black holes, representing a distinct phase in galaxy evolution. Due to severe dust obscuration, they appear faint in the optical and near-infrared (NIR) but exhibit strong emission in the mid-infrared (MIR) as heated dust re-radiates energy. Consequently, Hot DOGs are faint in the WISE W1 and W2 bands but prominent in W3 and W4. When coincident with nearby M-dwarfs along the line of sight, the coarse 6–12 arcsec resolution of WISE results in blended photometry that can mimic the SED of a cold Dyson Sphere. Notably, Blain (2024) estimated the Hot DOG occurrence rate in the WISE catalogue, concluding that their surface density is sufficient to explain all seven reported Dyson Sphere candidates as chance alignments.

For the remaining six Dyson Sphere candidates of Suazo et al. (2024), two have radio counterparts (Ren, Garrett & Siemion 2024) that are also likely to be AGNs (candidates A and B). The nature of the other four (candidates C, D, E, and F) is unclear. Subsequently, further identification of the optical spectra of the Project Hephaistos stars led to the ancillary discovery of three additional Dyson Sphere candidates (H, I and J), which show significant MIR excesses in the W3 and W4 bands (Suazo (2024) and Korn et al. (2026)).

Beyond searching for typical AGN signatures in potential background contaminants (*e.g.* high brightness temperature radio and X-ray emission), a complementary method involves identifying significant astrometric offsets across wavebands. By comparing WISE centroid positions with high-precision *Gaia* astrometry (accurate to microarcsecond scales), we can detect spatial offsets that serve as clear indicators of background contamination. This effect was explicitly observed in the analysis of Candidate G. Crucially, however, this approach relies on the background contaminant being spatially distinct from the foreground star; if the alignment is sufficiently precise, such offsets will remain unmeasurable. While Suazo et al. (2024) used W1 and W3 offsets to evaluate discrepancies and employed the Improved Reprocessing of the IRAS Survey (IRIS; Miville-Deschênes & Lagache 2005) maps at 100 μm to mitigate potential contamination, residual contamination still exists in some cases, as proved by the radio observation results of candidate G (Ren, Garrett & Siemion 2025). Owing to the limited spatial resolution of WISE and IRAS, directly measuring the offset between MIR centroids across the four WISE bands and *Gaia*-measured stellar positions provides a more effective and precise diagnostic for identifying extragalactic contamination in apparent infrared-excess sources, yielding the best constraint attainable from existing data before high-resolution imaging observations.

Supplementing the primary data from *Gaia* (Gaia Collaboration et al. 2016, 2023), 2MASS (Skrutskie et al. 2006), and WISE (Wright et al. 2010), deeper archival imaging surveys cover several of the nine targets. These include optical surveys such as the Dark Energy Survey (DES; Dark Energy Survey Collaboration et al. 2016; DES DR1: Abbott et al. 2018; DES DR2: Abbott et al. 2021), the Panoramic Survey Telescope and Rapid Response System (Pan-STARRS; Chambers et al. 2016), SkyMapper (Onken et al. 2024), and the DESI Legacy Imaging Surveys (Dey et al. 2019), as well as NIR surveys such as the VISTA Science Archive (Cross et al. 2012), and the WFCAM Science Archive (Hambly et al. 2008). The greater depth of these images provides a valuable independent diagnostic, offering clues to potential faint background extragalactic objects contaminating the MIR flux of the Dyson Sphere candidates. The culprits responsible for the excess, though absent in shallower surveys like SDSS and 2MASS, may be detectable in these high-sensitivity archival images.

This paper presents a comprehensive assessment of the Dyson Sphere candidates through two complementary approaches: an astrometric diagnosis based on positional offsets and a detailed inspection of deep photometric surveys. The paper is structured as follows: in Section 2, we briefly describe the data and methods used in this paper. We present the results of our astrometric diagnostics in Section 3, followed by the archival image examination results in Section 4. Finally, we discuss our findings in Section 5 and summarise our conclusions in Section 6.

2 DATA AND METHODS

2.1 *Gaia* Astrometry, Radio Counterparts, and *WISE* Centroid Measurement

We collected public archival data for nine M-dwarf candidates: six from Suazo et al. (2024) (S24 hereafter) and three from Suazo (2024) and Korn et al. (2026) (K26 hereafter), all of which have *Gaia* DR3 source identifiers (see Table 1). We retrieved their high-precision astrometry, including coordinates and proper motions, for all nine stars from the *Gaia* DR3 database. Using these positions, we searched for counterparts at complementary wavelengths. Radio counterparts for candidates A and B were found in the predecessor identification (Ren, Garrett & Siemion 2024) via the VizieR access tool (Ochsenbein et al. 2000), while candidates C–F and X-ray counterparts for all candidates remained undetected. In this work, we updated the VizieR query to account for new radio survey data and cross-matched all positions with the High Energy Astrophysics Science Archive Research Center (HEASARC) database[2], which similarly yielded no additional detections.

To prepare the data for MIR centroid analysis in Section 3, we retrieved $1' \times 1'$ image cutouts for each star in all four WISE bands from the ALLWISE atlas (WISE Team 2020) via the NASA/IPAC Infrared Science Archive (IRSA)[3]. To refine the centroid analysis, we manually measured the signal-to-noise ratios (SNRs) for the four *ALLWISE* band images of each source, rather than adopting the pipeline-generated SNR values in the *ALLWISE* catalogue (Cutri et al. 2021). We used the `sep.extract` method from SEP Python library (Barbary 2016), a re-implementation of SExtractor (Bertin & Arnouts 1996), to detect the centroids of the ALLWISE maps. The W1 and W2 images, which have significantly higher SNRs, can generally be fitted successfully with SEP. We evaluated several alternative methods for detecting WISE spatial centroids and determined that SEP generally yields the best performance. However, for lower-resolution W3 and W4 images where if SEP fails to provide a successful fit, we adopted the `scipy.ndimage.center_of_mass` (Virtanen et al. 2020) function.

Neither `sep.extract` nor `scipy.ndimage.center_of_mass` provides direct centroid position uncertainties. We estimated these using the standard photon-limited centroiding precision formula:

$$\sigma_{\text{position}} \approx \frac{\text{FWHM}}{k \times \text{SNR}} \tag{1}$$

where $k = 2\sqrt{2\ln 2} \approx 2.355$ (Howell 2006) converts between Full Width at Half Maximum (FWHM) and Gaussian σ. We adopted

[2] https://heasarc.gsfc.nasa.gov/
[3] https://irsa.ipac.caltech.edu/irsaviewer/

Table 1. Basic *Gaia* DR3 parameters of the Dyson Sphere candidate stars from Suazo et al. (2024), Suazo (2024), and Korn et al. (2026).

Candidate	Gaia DR3	RA, DEC (J2016.0)	G (Vega) (mag)	$T_{\rm eff}$ (K)	PM (mas yr^{-1})	pmRA (mas yr^{-1})	pmDEC (mas yr^{-1})	Plx (mas)	W1/W2 epoch	W3/W4 epoch	Selected surveys
A (J1245-2652)	3496509309189181184	12 45 12.9417, -26 52 03.276	15.996	3823	88.944	-5.717	-88.760	6.93	2010.516	2010.512	*Legacy* ($girz$); *VHS*(YJK_s)
B (J0356-4031)	4843191593270342656	03 56 03.8102, -40 31 48.524	17.713	3431	32.279	7.051	-31.500	4.68	2010.588	2010.579	*Legacy* ($girz$); *VHS*(JK_s)
C (J0456-7410)	4649396037451459712	04 56 03.0461, -74 10 14.156	18.393	3239	43.980	39.525	-19.288	4.54	2010.781	2010.294	*Legacy* ($girz$); *VMC*(YJK_s)
D (J2327+0506)	2660349163149053824	23 27 51.2948, +05 06 26.143	17.662	3473	37.522	-30.674	-21.611	4.70	2010.459	2010.456	*Legacy* ($girz$); UKIDSS ($YJHK$)
E (J0402-1054)	3190232820489766656	04 02 07.7970, -10 54 40.726	17.008	3557	45.385	33.957	30.112	3.62	2010.624	2010.107	*Legacy* (grz); *VHS*(YJK_s)
F (J0513-2511)	2956570141274256512	05 13 46.5124, -25 11 11.490	16.330	3674	23.643	11.575	-20.615	3.73	2010.164	2010.160	*Legacy* ($girz$); *VHS*(JK_s)
G (J2335-0004)	2644370304260053376	23 35 32.4891, -00 04 24.208	16.482	3481	68.699	-47.485	-49.646	3.97	2010.458	2010.455	*Legacy* ($girz$); *VHS* (JHK_s)
H (J2336-0920)	2437221214075471744	23 36 02.6653, -09 20 00.394	17.312	3418	28.321	-23.535	-15.753	3.68	2010.449	2010.446	*Legacy* ($girz$); *VHS*(YJK_s)
I (J0939+0700)	3854090071297359616	09 39 54.3199, +07 00 27.868	17.402	3327	15.504	-4.744	-14.760	5.89	2010.358	2010.354	*Legacy* ($girz$); UKIDSS ($YJHK$)
J (J0832+1442)	651765552072217216	08 32 16.5787, +14 42 18.557	16.133	3677	31.399	-5.615	-30.893	3.42	2010.823	2010.300	*Legacy* ($girz$); UHS (JHK)

Note. — All the candidates have complete Gaia astrometry and WISE photometry data. $T_{\rm eff}$ (Effective Temperature) is not available in *Gaia* DR3 for candidate A; we adopted its $T_{\rm eff}$ from *Gaia* DR2 instead. All the right ascension and declination positions are reported for the *Gaia* DR3 reference epoch J2016.0; PM, pmRA, pmDEC, and Plx denote the total proper motion, the proper-motion components in right ascension and declination, and the trigonometric parallax, respectively, as reported in *Gaia* DR3. All G-band magnitudes are reported on the Vega system. All optical and NIR band availabilities from selected surveys are presented, while the radio band information for A and B is described in Table 3.

WISE point spread function (PSF) FWHM of 6.1, 6.4, 6.5, and 12.0 arcseconds for W1–W4, respectively (Wright et al. 2010). The SNR at each centroid was manually measured via SEP aperture photometry. Therefore, all the centroiding uncertainties ($\sigma_{\rm position}$) can be derived through this formula.

2.2 Epoch Propagation and Proper Motion Corrections

The extracted *WISE* centroids and their associated positional uncertainties reflect the state of the MIR emission at the specific epoch of the observations. As summarised in Table 1, the *ALLWISE* epochs for our targets span J2010.0 to J2011.0. Even within the same survey, the W3 and W4 band data were often collected slightly earlier than the W1 and W2 data. Because our multi-wavelength dataset compiles images from multiple independent surveys, these epoch differences can be substantial. Consequently, we rigorously accounted for the proper motions of the target stars when examining and cross-matching the spatial centroids in Section 3.

In this context, the *Gaia* parallaxes in Table 1 span 3.42–6.93 mas and are negligible on the angular scales considered here. In contrast, the total proper motions range from 15.5 to 88.9 mas, yr^{-1}, with a median of 34.9 mas, yr^{-1}, corresponding to a displacement of approximately 0.35″ over 10 years. For instance, candidate A has a significant proper motion of 88.944 mas yr^{-1}. While its RACS-high radio image was obtained at J2022.518, its MIR images were acquired by WISE near J2010.5. This ~12 yr baseline introduces a purely kinematic positional displacement of 1.07″.

The *Gaia* DR3 astrometric solution is based on observations collected between 2014 and 2017, with the catalogue positions and proper motions referenced to epoch 2016.0. We therefore propagate the *Gaia* coordinates to the observing epoch of each individual image, preventing stellar proper motion from introducing spurious positional offsets. By applying this temporal alignment to every dataset, the uncertainty in each derived offset includes the centroiding uncertainty ($\sigma_{\rm position}$), together with the propagated positional and proper-motion uncertainties of the *Gaia* stellar source and, where applicable, the positional uncertainty of the corresponding radio counterpart.

2.3 Deep Optical and Near-Infrared Imaging Surveys

To examine the candidates using deep photometric and imaging data in Section 4, we queried several wide-field optical and NIR surveys, including the DES DR2, Pan-STARRS DR2, DESI Legacy Imaging Surveys (DR10), the UKIRT Infrared Deep Sky Survey (UKIDSS; Lawrence et al. 2007) and the UKIRT Hemisphere Survey (UHS; Dye et al. 2018) from the WFCAM Science Archive [4], and two VISTA programmes from the VISTA Science Archive [5]: the Hemisphere Survey (VHS; DR5, McMahon et al. (2013))) and the Magellanic Clouds Survey (VMC; DR6, Cioni et al. (2011)). Table 2 summarises the central/effective wavelengths (or frequencies) and nominal angular resolutions of the optical and infrared datasets used in this work, together with the RACS radio surveys (Hale et al. 2021; Duchesne et al. 2024, 2025) covering candidates A and B. We find that all candidates are covered by the Legacy DR10 Survey, which provides the ideal optical imaging and serves as the primary dataset for this study. Additionally, six candidate stars have available VISTA images: A, B, E, F, H from the VHS, and C from the VMC. All candidates without VISTA coverage are accounted for by the Infrared Deep Sky Survey (UKIRT): D and I are covered by UKIDSS, and J is covered by the UHS. These Legacy optical images, combined with the NIR data from VISTA or UKIRT surveys, provide deep, multi-band imaging across all candidate fields. This enables a visual diagnosis entirely independent of our mid-infrared centroid analysis.

To provide identifiers for newly discovered or faint objects in each candidate's images, we queried nearby NIR sources from the VISTA and UKIRT catalogues and optical sources from the Legacy DR10 Tractor catalogue. We also examined other major optical and NIR surveys, including DES, Pan-STARRS, SDSS, 2MASS, and SkyMapper. The DES images are already included in the DESI Legacy DR10 Imaging Surveys and thus are effectively represented in our Legacy analysis. The other surveys: Pan-STARRS, SDSS, 2MASS, and SkyMapper, have imaging quality and depth that are generally inferior to those of the Legacy, VISTA, and UKIRT datasets in the regions of interest. Our follow-up examination in Section 4 based on them did not yield additional detections of background or blended sources.

3 ASTROMETRIC DIAGNOSTICS

In this section, we analyse the positional offset between the MIR emission and the actual *Gaia* position for each candidate star. As demonstrated by Ren, Garrett & Siemion (2025), which analysed the case of candidate G, a significant offset between W3 & W4 emission spatial distribution to the star's coordinate is the indicator of

[4] http://wsa.roe.ac.uk/
[5] http://vsa.roe.ac.uk/

Table 2. Summary of the observational datasets used in this work. For each band we give the effective wavelength or central frequency and the nominal angular resolution, quoted as the full width at half-maximum (FWHM) of the synthesised beam for the radio surveys and of the point-spread function (PSF) for the optical and infrared imaging data. The final column gives the reference for each survey.

Survey (instrument)	Band	Effective Wavelength / Central Frequency ($\lambda_{\rm eff}/\nu_{\rm c}$)	FWHM ($''$)	Reference
ASKAP RACS	RACS-low	887.5 MHz	~25	Hale et al. (2021)
	RACS-mid	1367.5 MHz	~10	Duchesne et al. (2024)
	RACS-high	1655.5 MHz	~10	Duchesne et al. (2025)
Gaia (Astrometric Field)	G	0.64 μm	~0.10	Fabricius et al. (2016); Weiler (2018)
Legacy Survey	g	0.48 μm	1.3	Dey et al. (2019)
	r	0.64 μm	1.2	
	i	0.78 μm	~1.1–1.2	
	z	0.92 μm	1.1	
VISTA (VMC, VHS)	Y	1.02 μm	~0.8–1.0	Cioni et al. (2011); McMahon et al. (2013)
	J	1.25 μm		
	H	1.65 μm		
	K_s	2.15 μm		
UKIRT/WFCAM (UKIDSS, UHS)	Y	1.03 μm	~0.75–1.0	Lawrence et al. (2007); Dye et al. (2018)
	J	1.25 μm		
	H	1.63 μm		
	K	2.20 μm		
AllWISE	$W1$	3.4 μm	6.1	Wright et al. (2010)
	$W2$	4.6 μm	6.4	
	$W3$	12 μm	6.5	
	$W4$	22 μm	12.0	

background contamination. For clarity, we divide our nine candidates into three subsamples based on their properties and origin:

- Candidates A and B, which are found to have radio counterparts. We additionally compare the radio counterpart positions with the WISE centroids and the *Gaia* positions of the candidate stars.
- Candidates C, D, E, and F, the other four candidates drawn from S24 without radio counterparts.
- Candidates H, I, and J, the three newly identified targets from K26, also without radio counterparts.

The diagnostic process and results for each group are detailed in Subsections 3.1, 3.2, and 3.3. In Section 3.4, we compare the candidate centroiding results in this work with the offsets reported in S24. We then evaluate our astrometric approach in Subsection 3.5 by analysing control samples with W3 SNRs similar to those of the candidate stars.

3.1 Radio, WISE and Gaia astrometric diagnostics for candidates A and B

Candidates A (Gaia DR3 3496509309189181184) and B (Gaia DR3 4843191593270342656) are two of the three radio-associated sources (A, B, and G) reported by Ren, Garrett & Siemion (2024); the radio source associated with G has been confirmed as an AGN (Ren, Garrett & Siemion 2025). Candidates A and B are located in the southern sky, with associated radio sources detected in RACS-DR1 (Hale et al. 2021) at 887.5 MHz with an angular resolution of 25$''$. More recent RACS-mid (Duchesne et al. 2024) and RACS-high (Duchesne et al. 2025) observations at 1367.5 MHz and at 1655.5 MHz, provided significantly improved angular resolution compared to the original 25$''$ beam observations, enabling more precise comparison between radio source positions and stellar coordinates from Gaia. Figure 1 shows the positions of the radio sources A and B in different radio frequencies, and Table 3 shows the properties of the radio sources associated with candidate A and B.

Another supplementary dataset is the second data release for the GaLactic and Extragalactic All-sky Murchison Widefield Array eXtended (GLEAM-X)(Ross et al. 2024) which covers a frequency range of 72–231 MHz with twenty frequency bands. Although the angular resolution of GLEAM-X is at the arcminute level, it still effectively captures the fluxes of candidate B at lower frequencies. Combining GLEAM-X and RACS data extends the coverage from 87.5 to 1655.5 MHz. J0356-4031, the radio source associated with candidate B, has a high flux density exceeding 10 mJy at frequencies below 300 MHz and shows a steep radio spectral index (assuming a power-law radio spectrum $S_\nu \propto \nu^{-\alpha}$, where S_ν is the flux density, ν is the frequency, and α is the spectral index) of $\alpha_{87.5}^{1655.5} = 0.63 \pm 0.11$ (Figure 2). The radio source J1245-2652 associated with candidate A, detected only in RACS, has a less well-constrained radio spectral index of $\alpha_{887.5}^{1655.5} = 0.40 \pm 0.35$.

Using the *ALLWISE* centroid detection method described in Section 2, we obtained the MIR centroids for candidates A and B. All the W1, W2, and W3 band centroids were measured by the SEP, and both W4 images were measured by the SCIPY. These were then compared with their radio counterparts at 1367.5 MHz and 1655.5 MHz, a band that offers superior angular resolution and a circular beam. These WISE centroids were also compared with the stellar positions propagated to the *ALLWISE* epochs using *Gaia* DR3 proper motions, accounting for the time offset between the *ALLWISE* observations and the radio measurement epochs. Figure 3 shows the locations of the stars, radio sources, and MIR centroids, and Table 4 lists the measured offsets between the *Gaia*, radio, and WISE centroids for candidates A and B.

After accounting for proper motion, candidate A shows a $\sim 3.3''$ offset between the *Gaia* position of the star propagated to J2020.8 and the 887.5 MHz radio source. This is smaller than 4.9$''$ reported in Ren, Garrett & Siemion (2024), which did not correct for the star's proper motion. At higher frequencies with improved angular resolution (1367.5 MHz and 1655.5 MHz), the radio source to stellar offset reduces to ~1.2$''$ and ~1.6$''$ (Table 3). The W1 and W2 centroids

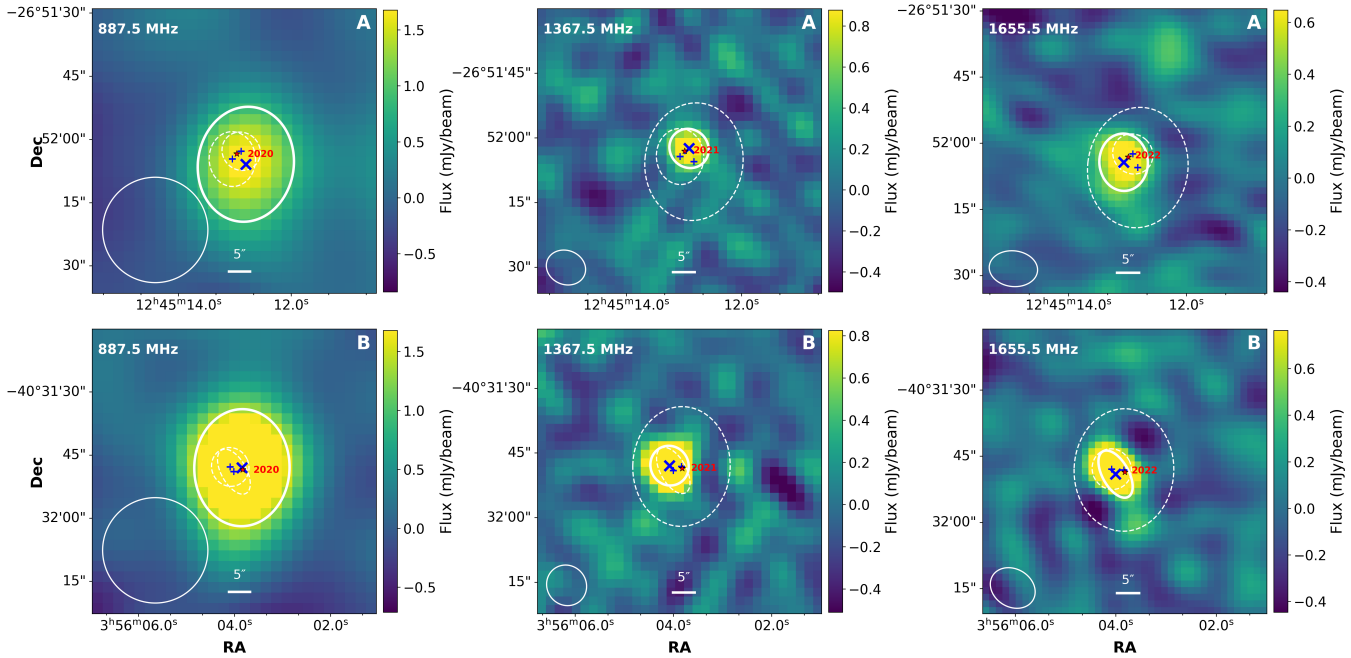

Figure 1. The Rapid ASKAP Continuum Survey (RACS) radio images of radio sources associated with candidates A (J1245-2652, top row) and B (J0356-4031, bottom row) are shown at three frequencies: 887.5 MHz (left), 1367.5 MHz (centre), and 1655.5 MHz (right), with each panel covering a field of view of 65 $''$ × 65 $''$. White ellipses show the PyBDSF source fits from the RACS catalogues, with thick solid lines indicating the fits at the frequency of the image, while thin dashed lines show fits from the other radio frequencies for comparison. Large blue crosses (×) mark radio source positions for the corresponding frequency, and small blue plus signs (+) indicate positions at other frequencies. The red stars represent the *Gaia* positions propagated to the corresponding RACS observation epochs using the measured proper motions.

Table 3. The properties of the radio source associated with candidates A and B.

Source	Survey (Epoch)	Central Freq. (MHz)	RA (J2000) (h m s)	Dec (J2000) (° ′ ″)	Flux Density (mJy)	Beam size (″ × ″ (°))	PyBDSF fit (″ × ″ (°))	Offset to star (″)	Weighted mean offset (″)
A (J1245-2652)	RACS-low (J2020.7917)	887.5	12 45 12.783	−26 52 06.20	1.75 ± 0.40	25.0 × 25.0 (0.0)	27.4 × 22.8 (171.8)	3.26 ± 2.03	1.27 ± 0.34
	RACS-mid (J2021.0490)	1367.5	12 45 12.864	−26 52 03.11	1.24 ± 0.31	9.3 × 7.9 (67.3)	9.4 × 8.8 (45.0)	1.18 ± 0.36	
	RACS-high (J2022.0518)	1655.5	12 45 13.022	−26 52 04.94	1.45 ± 0.39	11.0 × 8.1 (82.9)	13.0 × 11.0 (2.0)	1.59 ± 1.24	
B (J0356-4031)	GLEAM-X (J2020.0)	87.5	03 56 03.86	−40 31 48.8	11.43	186.9 × 152.4 (−53.2)	188.2 × 151.4 (−54.0)	0.58 ± 4.07	2.64 ± 0.36
		118.5			11.81	123.5 × 97.6 (−53.9)	123.5 × 96.0 (−54.0)		
		154.5			12.27	95.1 × 74.3 (−54.9)	97.5 × 72.2 (−54.0)		
		185.0			10.74	77.5 × 61.9 (−56.0)	80.5 × 59.4 (−54.0)		
		215.5			6.79	65.7 × 52.7 (−55.0)	69.1 × 49.7 (−54.0)		
	RACS-low (J2020.7924)	887.5	03 56 03.831	−40 31 48.19	2.90 ± 0.46	25.0 × 25.0 (0.0)	27.8 × 22.6 (178.3)	0.53 ± 1.41	
	RACS-mid (J2021.0179)	1367.5	03 56 04.074	−40 31 48.00	2.22 ± 0.29	9.6 × 9.1 (37.6)	9.3 × 8.8 (25.0)	3.05 ± 0.36	
	RACS-high (J2022.0645)	1655.5	03 56 03.998	−40 31 49.12	2.01 ± 0.35	10.7 × 8.6 (58.8)	11.8 × 6.0 (29.2)	2.14 ± 0.50	

Note. — Beam sizes are the synthesised beam FWHM, given as major axis × minor axis (″ × ″) and position angle (PA, °). PyBDSF fit sizes are the fitted source parameters (convolved with beam) from RACS catalogues (Hale et al. 2021; Duchesne et al. 2024, 2025) and GLEAM-X (Ross et al. 2024). The 'Offset to star' is the angular offset between the radio source position and the proper-motion (epoch) corrected *Gaia* DR3 position of the star. Radio-to-stellar offsets for GLEAM-X are calculated using the propagated *Gaia* position at epoch ∼2020.0; radio-to-stellar offsets for RACS are based on their epochs provided by the corresponding source catalogues. The 'Weighted mean offset' column gives the inverse-variance weighted average of the per-band offsets for each candidate.

lie ∼ 1.6″ and ∼ 1.5″ from the *Gaia* position propagated to J2010.5 of the candidate star A, respectively—closer than the corresponding offsets to the 1655.5 MHz radio source by over 2″, but still much larger than the offsets to the 1367.5 MHz source by ∼ 1.2″. In the W3 and W4 bands, the centroid–star offsets increase to about 2″, which exceed all centroid–radio offsets at 1367.5 MHz and 1655.5 MHz (both ∼ 1.6″). Combining the individual per-band measurements with inverse-variance weighting, the weighted-mean offset between the radio source and the epoch-corrected stellar (*Gaia*) position is 1.27 ± 0.34″ for candidate A and 2.64 ± 0.36″ for candidate B.

For candidate B, while the stellar-radio offset at 887.5 MHz is only ∼ 0.5″, observations with smaller beam sizes at 1367.5 MHz and 1655.5 MHz frequencies reveal significantly larger radio to stellar offsets exceeding 2″ (Table 3). Significantly, the WISE centroids at W3 bands are substantially displaced from star B's position by ∼ 2.8″, but align better with the 1367.5 MHz radio source location by only ∼ 0.5″ (Figure 3). In the W4 band with lower resolution than W3, the centroid is almost 4″ away from star B, while only ∼ 1″ from the 1367.5 MHz radio source.

3.2 Astrometric diagnostics for candidate C, D, E and F

.

We conducted the centroiding analysis for all four S24 candidate stars with no associated radio sources: C, D, E, and F. All W1 and W2 centroids for the four cases were obtained using SEP, while all

Table 4. *ALLWISE* W1 to W4 band emission centroid positions, centroiding uncertainties, and angular offsets (with uncertainties) to star positions in the *ALLWISE* epoch, and to the radio positions (1367.5 MHz and 1655.5 MHz) for candidates A and B.

Candidate	Band	RA (h m s)	Dec (d m s)	Centroiding Uncertainty (″)	Offset to star (″)	Offset to 1367.5 MHz (″)	Offset to 1655.5 MHz (″)
A (J1245-2652)	W1	12 45 12.945	−26 52 02.97	0.08	1.60 ± 0.08	1.09 ± 0.23	2.23 ± 0.95
	W2	12 45 12.951	−26 52 02.85	0.14	1.48 ± 0.14	1.19 ± 0.25	2.30 ± 0.97
	W3	12 45 12.971	−26 52 03.51	0.17	2.16 ± 0.17	1.49 ± 0.27	1.59 ± 0.97
	W4	12 45 12.991	−26 52 03.25	1.10	1.96 ± 1.09	1.71 ± 1.01	1.75 ± 1.48
	Weighted mean				1.66 ± 0.12	1.25 ± 0.14	2.01 ± 0.52
B (J0356-4031)	W1	03 56 03.831	−40 31 48.50	0.21	0.76 ± 0.20	2.81 ± 0.25	2.01 ± 0.36
	W2	03 56 03.886	−40 31 48.49	0.32	1.20 ± 0.27	2.20 ± 0.31	1.43 ± 0.41
	W3	03 56 04.042	−40 31 48.33	0.25	2.84 ± 0.19	0.49 ± 0.32	0.94 ± 0.37
	W4	03 56 04.140	−40 31 47.28	2.91	3.95 ± 2.23	1.04 ± 2.58	2.45 ± 2.65
	Weighted mean				1.73 ± 0.56	2.00 ± 0.55	1.48 ± 0.26

Notes. Throughout this paper, "Offset to the star" represents the angular separation between each MIR centroid and the corresponding *Gaia* position propagated to the corresponding *ALLWISE* epoch. This convention, featuring the red star as a reference marker, applies specifically to all WISE analysis maps (Figures 3, 4, and 5) throughout this paper. The "Weighted mean" row gives the inverse-variance weighted average of the W1–W4 offsets in each column; the uncertainty is scaled by $\sqrt{\chi^2/\mathrm{dof}}$ where the band-to-band scatter exceeds the formal errors.

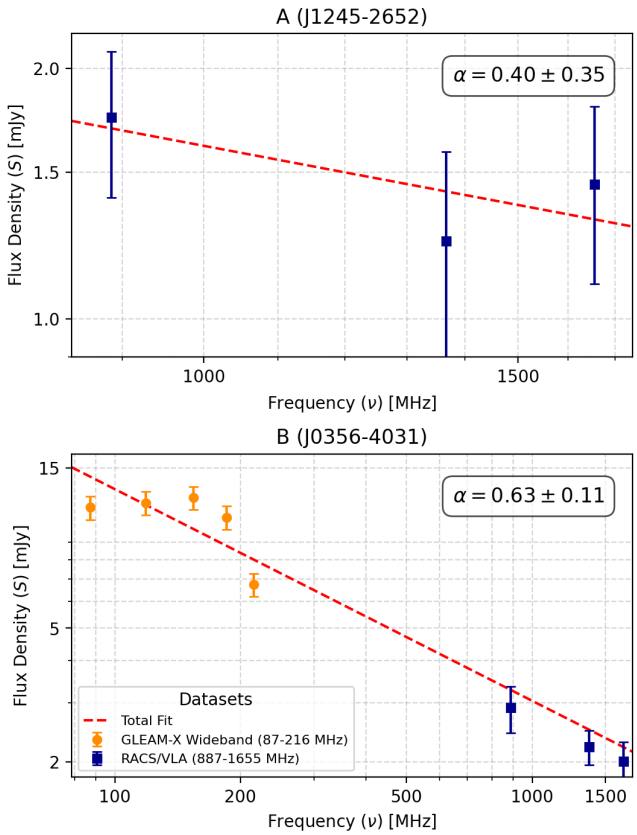

Figure 2. Radio spectral energy distributions and spectral index fits for candidates A (J1245-2652, top panel) and B (J0356-4031, bottom panel). Dark blue squares represent RACS-low, RACS-mid, and RACS-high observations at 887.5, 1367.5, and 1655.5 MHz. Orange circles in the bottom panel show GLEAM-X wideband integrated fluxes across five frequency channels (87.5, 118.5, 154.5, 185.5, and 215.5 MHz). The red dashed lines show power-law fits to the data, with spectral indices (α) derived via weighted least-squares fitting in log-space.

W4 images were fitted with `scipy`. For the W3 band, candidates C, D, and E were successfully fitted with SEP, but candidate F is elongated and could not be fitted by SEP, so we used `scipy` for its centroid. The astrometric results for these candidates are shown in Figure 4 and Table 5.

Candidate C (Gaia DR3 4649396037451459712) exhibits a positional offset between its W1&W2 emissions and W3&W4 emissions. As shown in Figure 4, the W3 and W4 emission centroids of candidate C are offset by ~ 3.7″ and ~ 5.0″, respectively, from the *Gaia* position propagated to J2010.3. In contrast, the W1 and W2 centroid offsets from the *Gaia* position propagated to J2010.8 are both < 1″.

For candidates D, E, and F, their W1 and W2 centroid-to-stellar offsets are all below 1″. Their W3 and W4 positional offsets are also less significant than those of C. Candidates D (Gaia DR3 2660349163149053824) and F (Gaia DR3 2956570141274256512) show relatively small stellar-to-centroid offsets in the W3 and W4 bands: their W3 centroids are all displaced by only ~ 0.7″, whereas the W4 centroids are by ~ 1.8″ (Table 5). However, the W4 detections for candidates D and F have only 3— 5σ significance above extended background structures, making the image quality insufficient to determine the true positional offsets in the W4 bands.

In contrast, candidate E (Gaia DR3 3190232820489766656) shows a larger centroid–stellar offset in both W3 and W4, with the emission centroids lying ~ 1.5″ north of the star. The W3 and W4 centroids themselves differ by ~ 1″, and the detections are significant at > 10σ and > 6σ, respectively. The above results for candidate E make its *ALLWISE* positional offset more reliable than those of candidates D and F, and less susceptible to low-SNR artefacts.

3.3 Astrometric diagnostics for candidate H, I and J

We present the astrometric analysis of the three new Dyson Sphere candidates in K26. None of these sources shows associated radio or X-ray sources based on our VizieR cross-match. The corresponding *ALLWISE* images and centroid measurements are shown in Figure 5 and Table 6.

In the W1 and W2 bands, three candidates were detected using SEP, and their MIR centroids show offsets below 1″. In the W3 and W4 bands, however, the MIR centroids—except for the W3 centroid of candidate H—were measured with `scipy`, as the image quality in

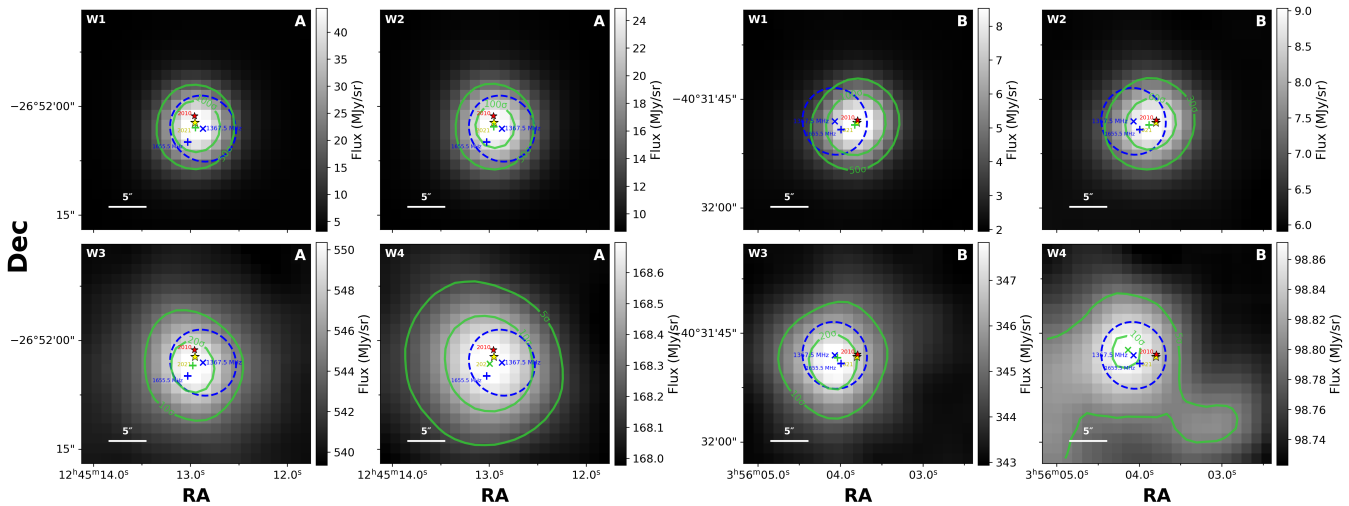

Figure 3. *ALLWISE* infrared images of radio source candidates A and B across four bands. Each subplot has a field of view of 30″ × 30″, with a 5″ scalebar provided for reference. Green contours show surface brightness at multiple σ levels above the background, where σ is the per-pixel background noise (RMS). Blue dashed ellipses and crosses mark the positions of the 1367.5 MHz radio sources, and the blue plus signs (+) mark the 1655.5 MHz radio sources. The red star and the underlying yellow star indicate the Gaia stellar positions corrected to the *ALLWISE* epoch and the RACS epoch (J2021), respectively. Green crosses (×) and plus signs (+) mark the infrared centroids. Candidate B's W1 and W2 centroids are offset from the radio source, while W3 and W3 are consistent, suggesting a background IR source. While candidate A appears to exhibit a higher degree of positional blending compared to candidate B.

Table 5. *AllWISE* MIR centroid positions, centroiding uncertainties, and offsets (with uncertainties) relative to the propagated *Gaia* positions at the *AllWISE* epoch for candidates C, D, E, and F.

Candidate	Band	RA (h m s)	Dec (d m s)	Centroiding Uncertainty (″)	Offset to the star (″)
C (J0456-7410)	W1	04 56 03.036	−74 10 13.95	0.25	0.82 ± 0.09
	W2	04 56 03.025	−74 10 13.87	0.40	0.76 ± 0.13
	W3	04 56 03.184	−74 10 10.36	0.27	3.67 ± 0.25
	W4	04 56 03.430	−74 10 09.39	2.43	4.98 ± 2.15
D (J2327+0506)	W1	23 27 51.319	+05 06 26.17	0.29	0.53 ± 0.19
	W2	23 27 51.332	+05 06 26.16	0.30	0.46 ± 0.30
	W3	23 27 51.389	+05 06 26.69	0.22	0.75 ± 0.22
	W4	23 27 51.357	+05 06 28.39	1.80	1.80 ± 1.80
E (J0402-1054)	W1	04 02 07.783	−10 54 40.66	0.16	0.88 ± 0.16
	W2	04 02 07.789	−10 54 41.06	0.26	0.68 ± 0.26
	W3	04 02 07.747	−10 54 39.89	0.24	1.50 ± 0.24
	W4	04 02 07.810	−10 54 40.19	2.26	1.52 ± 2.25
F (J0513-2511)	W1	05 13 46.524	−25 11 11.44	0.12	0.57 ± 0.11
	W2	05 13 46.536	−25 11 11.51	0.20	0.74 ± 0.19
	W3	05 13 46.539	−25 11 10.82	0.34	0.65 ± 0.31
	W4	05 13 46.632	−25 11 11.37	2.85	1.90 ± 2.59

these bands is too poor for reliable SEP detections. The W3 and W4 SNRs of candidates H, I, and J are generally low; only the W3 image of candidate J reaches a detection significance above 5σ.

Candidate H (Gaia DR3 2437221214075471744) shows a $\sim 2\sigma$ W3 detection with a centroid displaced by $\sim 2.6''$ from the *Gaia* position of the star propagated to J2010.4. In the W4 band, the source appears elongated, showing a centroid-to-stellar offset of $\sim 1''$. The detailed spatial structure of this elongated source in the W4 band is obscured due to the low image quality.

Similarly, the W3 and W4 images of candidates I and J exhibit elongated brightness profiles. Candidate I (Gaia DR3 3854090071297359616) appears as an extended stripe in W3, possibly arising from blended emission associated with multiple nearby sources, and is detected at only $\sim 2\sigma$. In W4, the source exhibits a smoother morphology with a significance of $\sim 3\sigma$. For W3, we derived the centroid using the southeastern peak emission, which is closest to the *Gaia* position of candidate star I propagated to J2010.4. The resulting W3 and W4 centroids lie more than 2″ and 3″ from the J2010.4 *Gaia* position, respectively. These centroids are oriented in nearly opposite directions, differing by over 5″. The W4 centroid is offset by $\sim 3.2''$ from the star I, showing a pattern similar to that seen for candidate C.

Candidate J (Gaia DR3 6517655520722172 16) also shows an offset between the W3 and W4 centroids. Its centroid-to-stellar offsets are $\sim 2''$ in W3 and $\sim 6''$ in W4, with opposite directions—the W3 and W4 centroids of candidate J are separated by more than 7″, appearing as if W3 and W4 are dominated by two different MIR sources.

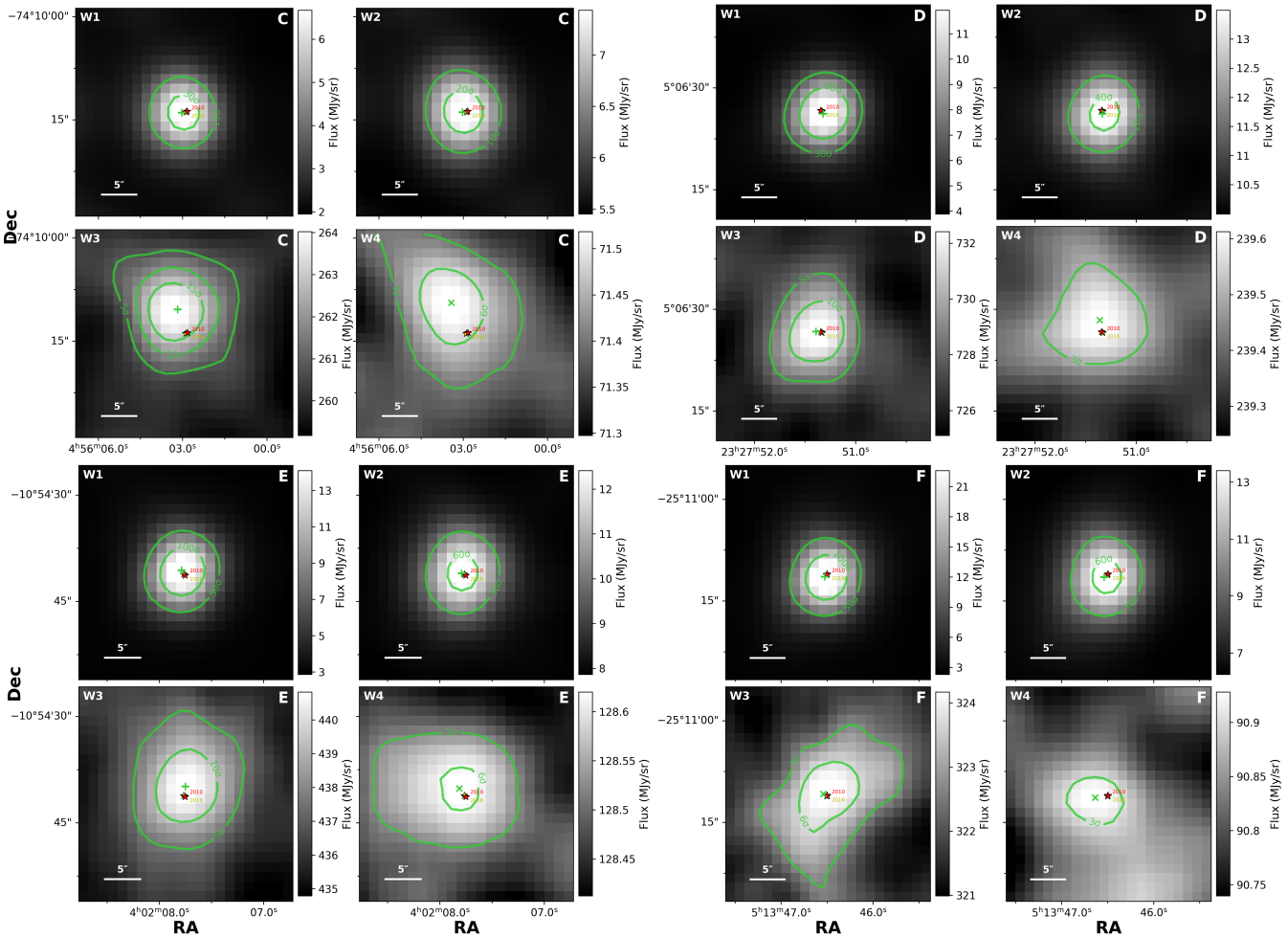

Figure 4. *ALLWISE* infrared images of the radio-undetected candidates C, D, E, and F across four bands. Each subplot has a field of view of 30″ × 30″, with a 5″ scalebar provided for reference. Green contours show surface brightness at multiple σ levels above the background, where σ is the per-pixel background noise (RMS), and the Green crosses (×) and plus signs (+) mark the MIR centroids. The red star and the underlying yellow star indicate the Gaia stellar positions corrected to the ALLWISE epoch and the Gaia DR3 epoch (2016.0). For the four sources, candidate C appears to have positional offsets between different WISE bands similar to the pattern of Candidate B, while the MIR centroids and star positions in candidates D, E, and F appear more blended.

Table 6. *AllWISE* MIR centroid positions, centroiding uncertainties, and offsets (with uncertainties) relative to the propagated *Gaia* positions at the *AllWISE* epoch for candidates H, I, and J.

Candidate	Band	RA (h m s)	Dec (d m s)	Centroiding Uncertainty (″)	Offset to the star (″)
H (J2336-0920)	W1	23 36 02.707	−09 20 00.560	0.19	0.55 ± 0.19
	W2	23 36 02.694	−09 20 00.066	0.34	0.38 ± 0.34
	W3	23 36 02.834	−09 20 01.461	0.53	2.63 ± 0.53
	W4	23 36 02.733	−09 20 00.496	2.37	0.89 ± 2.34
I (J0939+0700)	W1	09 39 54.337	+07 00 27.928	0.16	0.24 ± 0.16
	W2	09 39 54.344	+07 00 27.746	0.27	0.40 ± 0.27
	W3	09 39 54.315	+07 00 25.856	0.62	2.10 ± 0.62
	W4	09 39 54.239	+07 00 30.934	2.15	3.22 ± 2.15
J (J0832+1442)	W1	08 32 16.575	+14 42 18.643	0.11	0.11 ± 0.11
	W2	08 32 16.575	+14 42 18.751	0.20	0.09 ± 0.19
	W3	08 32 16.694	+14 42 17.700	0.33	1.94 ± 0.33
	W4	08 32 16.694	+14 42 24.985	2.17	6.46 ± 2.17

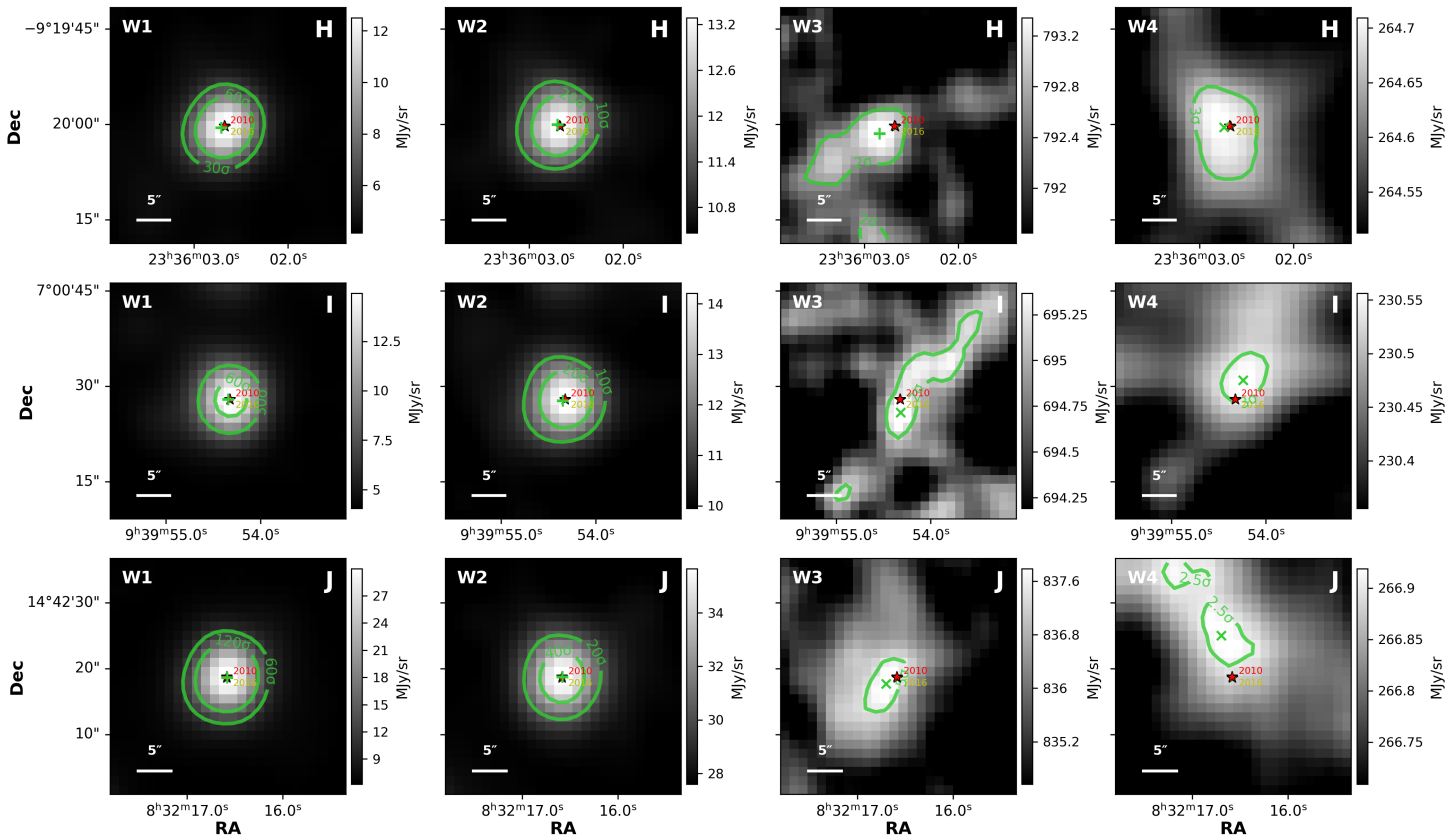

Figure 5. *ALLWISE* infrared images of candidate stars H, I, and J across four bands. Each subplot has a field of view of 36″ × 36″, with a 5″ scalebar provided for reference. Green contours show surface brightness at multiple σ levels above the background, where σ is the per-pixel background noise (RMS), and the Green crosses (×) and plus signs (+) mark the MIR centroids. The red star and the underlying yellow star indicate the *Gaia* stellar positions corrected to the *ALLWISE* epoch and the Gaia DR3 epoch (2016.0). Three candidates generally exhibit lower W3 and W4 SNRs compared to A–F. Among these, only the W4 emission for candidate H appears positionally aligned; all other W3 and W4 detections show apparent offsets, with the W3 flux for candidate I notably displaying an extended strip.

3.4 Comparison with the Photocentre for the S24 Candidate Stars

Candidates A and B in Subsection 3.1 and C, D, E, and F in Subsection 3.2 were analysed for photocentre offsets in S24. Although our centroiding methods are not identical to those used in S24, our results are broadly consistent with the values presented in Table 7 of S24. Our calculated W1/W2 total offsets remain below 0.5″. For candidates B and C, the W1/W3 total offsets of 2.43″ and 3.64″ align with the significant displacements reported for those cases in S24. Table 7 presents a comparison between the results from S24 and this work.

For the remaining candidates (A, D, E, and F), W1/W3 positional offsets range from 0.7″ to 1.2″. These do not deviate from the broad distributions suggested in Theissen & West (2017) ($\sigma \approx 5''$), where band-to-band centroiding was applied to investigate warm dust around M dwarfs. While utilising precise *Gaia* DR3 positions in this work provides a better stellar reference, it does not inherently mitigate the degeneracy caused by such wide statistical ranges. To better examine the potential background contaminants of the candidate stars, we selected sets of SNR-matched control stars for a comparative analysis, as detailed in Section 3.5.

3.5 ALLWISE Image Centroid Analysis of Ordinary M-Dwarf Control Stars

To evaluate the statistical significance of our astrometric offsets, we constructed nine distinct control groups—one corresponding to each of the investigated candidates from A to J, except for candidate G, as it was previously identified as a clear case of AGN contamination (Ren, Garrett & Siemion 2025).

We first construct an initial parent sample of ordinary M-dwarfs by selecting sources from *Gaia* DR3 with a Renormalised Unit Weight Error (RUWE) < 1.4 located within 300 pc. To specifically isolate the M-dwarf population, we applied multiple astrophysical constraints, including an absolute magnitude cut of $M_G > 7.7$, an effective temperature threshold of $T_{\rm eff} < 4000$ K, and a colour cut of $G_{\rm BP} - G_{\rm RP} \geq 1.84$ (Montalto et al. 2021). Following cross-matching with the 2MASS and *AllWISE* catalogues, this initial selection yielded approximately 2 million sources.

Subsequently, we applied a series of stringent *AllWISE* photometric quality filters to ensure the reliability of the MIR detections. We required a signal-to-noise ratio SNR > 3 in both the W3 and W4 bands, a criterion that excluded over 99 per cent of the sources. Additionally, we imposed profile-fit χ^2 limits (w3rchi2 < 1.05 and w4rchi2 < 1.3), mandated the absence of saturation, and required at least one valid profile-fit measurement in both the W3 and W4 bands.

Table 7. Comparison of photocentre offsets (arcsec) between S24 and this work.

Candidate	W1/W2 Offset (RA/Dec; ″)		W1/W3 Offset (RA/Dec; ″)		W2/W3 Offset (RA/Dec; ″)
	S24	This Work	S24	This Work	This Work
A (J1245-2652)	−0.25/−0.01	0.00/0.01	−0.03/0.33	0.33/−0.65	0.33/−0.66
B (J0356-4031)	0.40/0.31	0.63/0.03	3.21/0.06	2.43/0.15	1.80/0.12
C (J0456-7410)	0.25/−0.32	−0.05/0.08	1.52/−3.68	0.77/3.56	0.81/3.48
D (J2327+0506)	−0.31/−0.12	0.19/−0.01	0.60/−0.09	1.05/0.52	0.85/0.53
E (J0402-1054)	−0.09/0.48	0.10/−0.40	−1.15/−0.38	−0.52/0.73	−0.62/1.13
F (J0513-2511)	0.03/0.10	0.19/−0.08	−1.04/0.79	−0.08/1.18	−0.27/1.26

Collectively, these requirements reduced the parent population to a final baseline sample of 3,582 high-quality ordinary M-dwarfs (see Table 8).

To establish a reliable astrometric baseline, we matched stars based on their *Gaia* DR3 G-band magnitudes, W1 SNR, and W2 SNR. This selection relies on the premise that at these shorter wavelengths, corresponding to the Rayleigh–Jeans tail, the SEDs of potential Dyson Sphere candidates should remain similar from ordinary M-dwarfs. This matching criterion initially yielded 406 stars selected from the parent sample of 3,582. We then performed a direct visual inspection to ensure clear profile structures in the W3 and W4 bands, filtering the sample down to 155 final control stars across the nine groups (see Table 9).

We then performed a centroid analysis on the 155 stars, following the same procedure introduced in Section 2 and applied in Subsections 3.1, 3.2, and 3.3. For each star where a centroid was successfully detected, the centroiding process yielded both a positional offset and the corresponding uncertainty. The positional offsets of the control stars, used as the reference for the candidate stars, are then quantitatively analysed using the Rayleigh distribution by employing `scipy.stats.rayleigh`, with the quantitative results presented in Table 10.

The typical offset scale of the M dwarfs in each band of each control sample is characterised by the Rayleigh scale parameter $\sigma_{\rm R}$. Each candidate's offset $r_{\rm cand}$ is compared against this scale to determine a Rayleigh survival probability $p_{\rm R}$, which represents the chance of a control star showing an offset at least as large. We then recast this probability as a one-sided Gaussian-equivalent significance, $\Phi^{-1}(1-p_{\rm R})$, which enables the standard-deviation expression. For all control samples, we also calculate an outlier-insensitive median scale $\sigma_{\rm med}$ as an independent baseline. This serves as a reliable backup because some datasets, most notably the W3 and W4 bands, do not strictly follow a Rayleigh distribution. As shown in Table 10, several cases (the W1 and W2 bands of C, and the W2 band of F) that are not significant under the Rayleigh scale reach $> 2\sigma$ Gaussian-equivalent significance under the median scale. Appendix A presents further details of the Rayleigh-distribution analysis beyond the table, including the full centroid-offset distributions for all candidates and bands and an example of the control-star centroiding for candidate A.

Candidate A is the clear standout of the quantitative analysis in Table 10. In both its W1 and W2 bands, the Rayleigh fits yield $p_{\rm R} < 1\times10^{-10}$ and a Gaussian-equivalent significance of $> 6\sigma$, indicating that its W1/W2 WISE centroids deviate strongly from clean M-dwarf behaviour. Whether this reflects an unrecognised background galaxy, an unusual debris configuration, or a genuine waste heat technosignature, the centroid profile of A is statistically distinct from the normal M-dwarf population in W1 and W2.

Among the other candidates, the next most significant after A are the W2 band of B (Gaussian-equivalent significance 3.7σ) and the W1 band of E (3.3σ). A marginal case is the W1 band of candidate B, with a Gaussian-equivalent significance of 2.3σ; here the median-scale baseline suggests a higher value of 4.3σ, indicating an anomalous offset discrepancy between candidate B and its control stars in the W1 band offsets. Similarly, the W1 and W2 bands of C and the W2 band of F show no significant deviation under the Rayleigh scale but reach Gaussian-equivalent significances of 3.1σ, 2.6σ and 2.7σ under the median scale, respectively (Table 10). However, across all bands, the centroid-to-stellar offsets for candidates D, H, I, and J do not behave as anomalies under either of the two quantitative analysis methods.

4 ARCHIVAL IMAGE DIAGNOSTICS

To identify potential background contaminants that escape detection in the *Gaia*, *2MASS* and *WISE* surveys with shallower depth, we utilise deep archival optical and NIR photometric data. In the optical regime, all candidates are covered by the deep DESI *Legacy* Survey DR10 imaging, which offers superior depth compared to shallower surveys (e.g., *SDSS*, *SkyMapper*, and *Pan-STARRS*). In the NIR regime, coverage varies depending on the specific survey footprints: A, B, E, F, and H are imaged by the *VHS* surveys, while only candidate C is covered by the *VMC* surveys. The remaining three candidates lack VISTA imaging but are instead covered by UKIRT surveys, with D and I observed by UKIDSS and J captured by the UHS. Consequently, we divide the sample into three groups based on their available near-infrared survey coverage:

- Candidates A, B, E, F, and H (with VHS coverage);
- Candidate C (with VMC coverage);
- Candidates D, I, and J (with UKIDSS or UHS coverage).

We complement our image inspection by examining the associated VISTA and UKIRT catalogues in the NIR regime, and *DESI Legacy* DR10 *Tractor* optical catalogues to find identifiers and existing photometric classifications for sources apparent in the images of each candidate. The VISTA and UKIRT catalogues provide basic stellar/galaxy morphological classifications, and the *Legacy Tractor* catalogue offers detailed brightness profile types (PSF, REX, EXP, etc.) and properties. The combined optical and NIR data approach enables us to diagnose the nature of the associated sources preliminarily.

To identify potentially uncatalogued radio sources that might indicate AGN contamination, we also inspected archival radio imaging, including the NRAO VLA Sky Survey (NVSS; Condon et al. 1998), the Faint Images of the Radio Sky at Twenty-Centimeters (FIRST; Becker et al. 1995), the VLA Low-frequency Sky Survey Redux (VLSSr; Lane et al. 2014), and the Sydney University Molonglo Sky Survey (SUMSS; Mauch et al. 2003), for sources lacking radio catalogue counterparts. No new radio candidates with significance exceeding 3σ were identified.

We applied the imaging and photometric inspection method to

Table 8. Summary of the selection criteria used to construct the M-dwarf control sample.

Step	Filter criterion	Source count
	Initial Sample Selection	
1	*Gaia* DR3 RUWE < 1.4 and distance < 300 pc	6,346,475
	M-dwarf Selection	
2	Absolute magnitude $M_G > 7.7$ (pass rate: 85%)	—
	2MASS and *AllWISE* best-neighbour match (pass rate: 61%)	—
	$T_{\rm eff} < 4000$ K and BP − RP ≥ 1.84 (pass rate: 61%)	2,016,459
	Photometric Quality Selection	
3	Both W3 and W4 S/N > 3 (pass rate: 1%)	
	Profile-fit χ^2: w3rchi2 < 1.05 and w4rchi2 < 1.3 (pass rate: 88%)	
	No saturation: w3sat = 0 and w4sat = 0 (pass rate: 97%)	3,582
	Number of measurements: w3nm > 0 and w4nm > 0 (pass rate: 30%)	

Table 9. The candidate star properties and the corresponding control sample selection. The left section lists properties for the candidate stars, while the right section defines the selection criteria and resulting sample sizes for the control groups. SNR values are taken from *AllWISE* catalogue and G-band Vega magnitudes are from *Gaia* DR3. $N_{\rm sel}$ shows the number of control stars that passed the SNR and G-magnitude selection, while $N_{\rm fit}$ denotes the number of control stars that passed the visual check and were therefore used for the Rayleigh distribution analysis.

Candidate	Candidate Star			Control Sample (M-dwarfs)				
	$\mathrm{SNR_{W1}}$	$\mathrm{SNR_{W2}}$	G-mag	W1 Range	W2 Range	G-mag Range	$N_{\rm sel}$	$N_{\rm fit}$
A (J1245−2652)	45.8	48.2	15.996	44.8–46.8	47.2–49.2	15.75–16.25	25	15
B (J0356−4031)	43.7	39.5	17.713	41.7–45.7	37.5–41.5	17.20–18.20	58	20
C (J0456−7410)	41.8	33.3	18.393	39.8–43.8	31.3–35.3	17.90–18.90	28	16
D (J2327+0506)	41.9	31.4	17.662	39.9–43.9	29.4–33.4	17.20–18.20	29	13
E (J0402−1054)	43.3	38.4	17.008	41.3–45.3	36.4–40.4	16.50–17.50	94	25
F (J0513−2511)	44.0	42.4	16.330	42.0–46.0	40.4–44.4	15.80–16.80	95	37
H (J2336−0920)	41.6	29.5	17.312	39.6–43.6	27.5–31.5	16.30–18.30	23	9
I (J0939+0700)	44.4	34.9	17.402	42.4–46.4	32.9–36.9	16.90–17.90	26	9
J (J0832−1442)	44.7	32.6	16.133	40.0–45.0	28.0–38.0	15.00–17.00	28	11

candidate G as a verification case, utilising its Legacy Survey DR1, *VHS* and *UHS* data; the findings are described in Subsection 4.1. The diagnostic results for the three groups, derived from archival image inspections, follow in Subsections 4.2, 4.3, and 4.4.

4.1 Searching for the AGN associated with Candidate G in the Optical and NIR regimes

To validate the effectiveness of detecting background contaminants using deep archival imaging, we first apply our analysis methodology to the hot DOG associated with candidate G (J2335–0004). This object was recently confirmed as a radio-loud AGN by Ren, Garrett & Siemion (2025) using VLBI astrometry, and the *ALLWISE* positional offset analysis supports its hot DOG properties. We examined the same archival *Legacy*, *VISTA* and *UKIRT* survey datasets used for the nine new candidates to determine if this known contaminant could be identified solely through archival inspection.

J2335-0004 was effectively detected by the DESI *Legacy* Survey. The *Legacy* DR10 Tractor catalogue suggested that this object has an REX profile, consistent with an extended source (a galaxy). It is notably faint across optical bands, with g, r, i, and z AB magnitudes of 24.43, 24.23, 24.20, and 23.11 mag, respectively. This *Legacy* object in the optical regime is located 0.28″ away from the AGN core position of J2335-0004 (23:35:32.8406, -0:04:25.069) detected through the EVN (e-VLBI) by Ren, Garrett & Siemion (2025).

In the *VHS* survey, J2335–0004 was reported to be an extended, galaxy-like source, with a $\mathrm{K_s}$-band AB magnitude of 19.89 ± 0.26 mag. Additionally, the *VHS* DR5 catalogue (McMahon et al. 2013) reported a double detection at this location: VHS J233532.82-000424.9 and VHS J233532.84-000425.2. Both detections are found to be highly coincident, lying ∼ 0.3″ away from the AGN core position of J2335-0004. In another NIR survey, this source was catalogued in the UKIDSS DR9 Large Area Survey (Lawrence et al. 2007) as ULAS J233532.83-000425.1; it is classified as a galaxy-like object with a K-band AB magnitude of 20.09 ± 0.21 mag.

We also inspected archival image data from the SkyMapper, Pan-STARRS, and SDSS; however, the faint optical magnitude (as revealed by the *Legacy* DR10 catalogue) falls below their respective detection thresholds, and we did not find its presence. These findings on the AGN companion of candidate G effectively demonstrate that deep public archival surveys can identify background contaminants at minimal cost, if their depth and sensitivity are adequate. However, this archival evidence alone is insufficient for a complete MIR contributor diagnosis. A further astrometric analysis, similar to that performed in Section 3, is required to confirm that the MIR emission is genuinely contributed by the background galaxy revealed in the archival images.

4.2 Image diagnostics for candidate A, B, E, F, and H

The five candidates covered by the VHS survey include A and B, both of which have radio counterparts in the public surveys, and E, F, and H, which show no associated radio emission.

Figure 7 presents the *VHS* $\mathrm{K_s}$-band and *Legacy* DR10 g-band images for candidates A and B, the two sources with confirmed radio counterparts. For candidate A, we find a significant spatial coincidence between the *WISE* W3 and W4 centroids, the 1367.5 MHz and 1655.5 MHz radio positions, and the central optical/NIR source brightness profile in Figure 7. The source maintains a consistent, unresolved morphology across all available archival bands (*VHS J*

Table 10. Rayleigh-distribution analysis of centroid offsets for the candidate control samples (W1–W4). N is the number of valid control stars; σ_R is the Rayleigh scale of the control sample, where the Rayleigh distribution peaks at (illustrated in Fig. A2); p_R is the Rayleigh survival probability at the candidate offset; and the Gaussian-equivalent significance is the one-sided σ transformed from p_R. The Note column flags bands anomalous ($> 3\sigma$) or marginal (2–3σ); "median" entries represent the significance under an alternative median scale $\sigma_{\rm med}$ for some cases.

Candidate	Band	N	Rayleigh scale σ_R **(arcsec)**	Rayleigh survival probability p_R	Gaussian-equivalent significance (Rayleigh) (σ)	Note
A (J1245−2652)	W1	15	0.17 ± 0.03	4×10^{-19}	8.86 ± 1.54	Anomalous ($> 3\sigma$)
	W2	15	0.21 ± 0.04	3×10^{-11}	6.55 ± 1.37	Anomalous ($> 3\sigma$)
	W3	15	1.50 ± 0.27	0.355	0.37 ± 0.58	
	W4	9	3.29 ± 0.77	0.837	-0.98 ± 1.50	
B (J0356−4031)	W1	19	0.26 ± 0.04	0.012	2.26 ± 1.41	Marginal; 4.3σ under the median scale $\sigma_{\rm med}$
	W2	19	0.28 ± 0.05	1×10^{-4}	3.66 ± 1.18	Anomalous ($> 3\sigma$)
	W3	18	2.29 ± 0.38	0.463	0.09 ± 0.29	
	W4	9	2.80 ± 0.66	0.371	0.33 ± 1.96	
C (J0456−7410)	W1	14	0.33 ± 0.06	0.048	1.66 ± 1.08	3.1σ under the median scale $\sigma_{\rm med}$
	W2	14	0.35 ± 0.07	0.091	1.33 ± 0.72	2.6σ under the median scale $\sigma_{\rm med}$
	W3	12	2.59 ± 0.53	0.367	0.34 ± 0.33	
	W4	7	2.74 ± 0.73	0.192	0.87 ± 1.69	
D (J2327+0506)	W1	13	0.33 ± 0.06	0.276	0.59 ± 1.39	
	W2	13	0.35 ± 0.07	0.425	0.19 ± 2.35	
	W3	10	2.39 ± 0.53	0.952	-1.66 ± 0.36	
	W4	5	3.30 ± 1.04	0.862	-1.09 ± 2.76	
E (J0402−1054)	W1	25	0.23 ± 0.03	5×10^{-4}	3.29 ± 0.94	Anomalous ($> 3\sigma$)
	W2	25	0.30 ± 0.04	0.071	1.47 ± 1.29	
	W3	20	2.57 ± 0.41	0.843	-1.01 ± 0.31	
	W4	14	2.48 ± 0.47	0.828	-0.95 ± 3.40	
F (J0513−2511)	W1	36	0.53 ± 0.06	0.562	-0.16 ± 1.00	
	W2	37	0.46 ± 0.05	0.275	0.60 ± 1.05	2.7σ under the median scale $\sigma_{\rm med}$
	W3	28	2.28 ± 0.30	0.960	-1.75 ± 0.98	
	W4	21	2.99 ± 0.46	0.817	-0.91 ± 3.31	
H (J2336−0920)	W1	7	0.56 ± 0.11	0.618	-0.30 ± 0.79	
	W2	7	0.51 ± 0.07	0.760	-0.71 ± 2.71	
	W3	5	3.54 ± 0.92	0.759	-0.70 ± 0.48	
	W4	4	2.35 ± 0.83	0.931	-1.48 ± 3.69	
I (J0939+0700)	W1	7	0.16 ± 0.04	0.336	0.42 ± 2.65	
	W2	7	0.16 ± 0.03	0.037	1.78 ± 3.25	
	W3	3	1.94 ± 0.29	0.557	-0.14 ± 0.66	
	W4	6	2.53 ± 0.73	0.444	0.14 ± 2.41	
J (J0832−1442)	W1	10	0.29 ± 0.07	0.933	-1.50 ± 2.58	
	W2	10	0.38 ± 0.09	0.973	-1.92 ± 3.17	
	W3	9	1.49 ± 0.29	0.429	0.18 ± 0.50	
	W4	5	2.93 ± 0.93	0.088	1.35 ± 1.05	

and Y; *Legacy* r, i, and z). The associated *VHS* and *Legacy Tractor* catalogues don't show any companion objects within a 10″ distance from candidate A.

For candidate B, as revealed by Section 3.1, the 1367.5 MHz and 1655.5 MHz radio counterparts, along with the *WISE* W3 and W4 centroids, are tightly clustered ∼ 3″ to the east of the candidate star B. This position does not exhibit significant emission in the *VHS* K_s-band image (Figure 7) and is not detected in the other available *VHS* bands. Furthermore, no close companion source is catalogued at this position in either the *VHS* or *Legacy* DR10 Tractor catalogues. However, the *Legacy* g-band image reveals a faint, tail-like structure at this offset location, consistent with the radio and *WISE* positions, detected with a peak significance of $\sim 4.7\sigma$.

As for the remaining candidates, E and F show conditions similar to candidate A (Figure 8). They exhibit W3 and W4 centroids that are spatially coincident with the brightness profiles of the central stars. Additionally, no other objects appear to be located within the regions of MIR flux.

Candidate H presents a more complex morphology. While its W4 centroid aligns with the central stellar source, the W3 centroid is significantly offset by ∼ 2.6″, placing it outside the star's main brightness profile. Unlike candidate B, the multi-band images of candidate H do not reveal obvious extended structures or 'tails' that clearly indicate a companion. However, inspection of the *Legacy* DR10 data reveals a faint source with a PSF-like profile (DESI Legacy ID 10995408501213714) located ∼ 5″ to the northeast (Figure 8). This object, likely a distant galaxy, coincides with the high-flux region of the W4 emission and lies on the fringe of the W3 emission.

4.3 Image diagnostics for candidate C

Candidate C is the only case covered by the *VMC* survey, and it lacks any associated radio or X-ray counterparts from archival data. Figure 9 shows its *VMC* J, Y, and K_s band images, and the *Legacy* DR10 r, i, and z band images. A critical finding is the presence of an extended tail-like structure located to the north of the central star, with a peak emission reaching a significance of 6.1σ. This tail corresponds to the catalogued source VMC J045603.25-741010.66, detected as a faint extended source with a K_s-band AB magnitude of 21.60 ± 0.32 mag. The morphological analysis in the VISTA Magellanic Survey (VMC) catalogue (YJK_s) DR6 (Cioni et al. 2011)

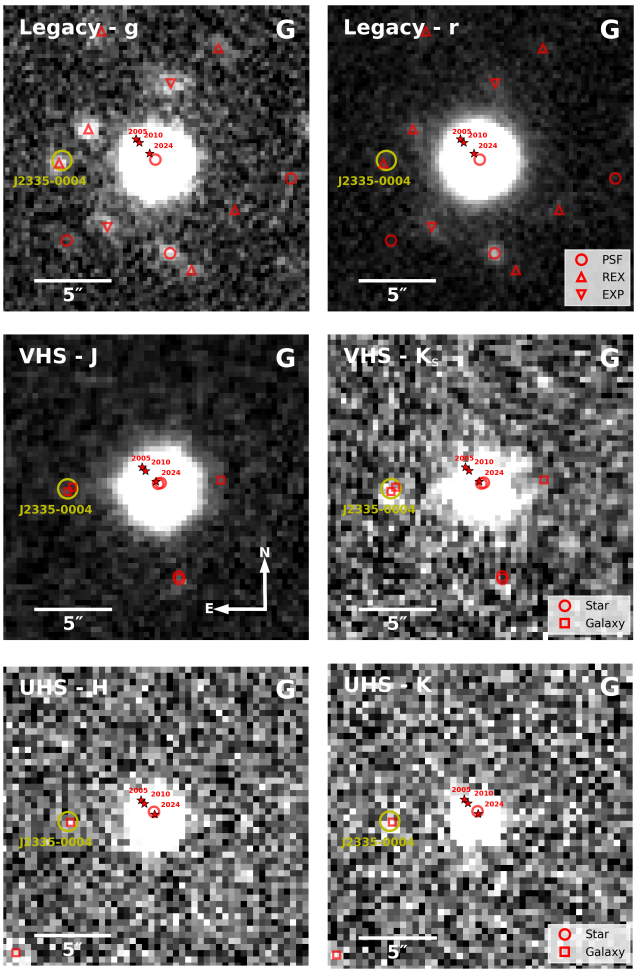

Figure 6. *Legacy* DR10 g- and r-band images (upper panels), *VHS* J- and K_s-band images (middle panels), and *UHS* H- and K-band images (lower panels) for candidate G. Red stars mark the propagated *Gaia* positions in 2005, 2010, and 2024, and the yellow circles indicate the AGN core position detected by EVN (e-VLBI). In the *Legacy* g band panels, red circles indicate sources with PSF profiles, while red triangles mark REX sources using upward triangles and mark EXP sources using downward triangles. In the *VHS* and *UHS* panels, red circles show stellar objects from the *VHS* catalogue, and the green squares mark the galaxy-like objects. A compass marker in the bottom-right of the middle-left panel (VHS–J) indicates orientation (N/E) for all subplots.

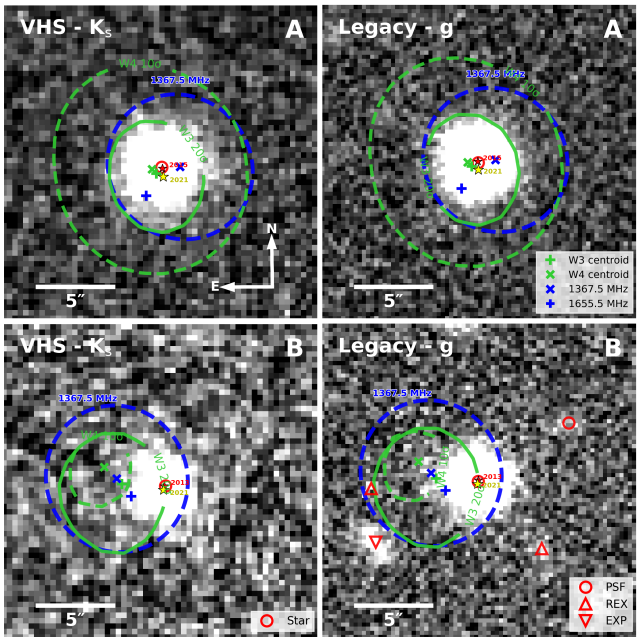

Figure 7. *VHS* K_s-band (left panels) and *Legacy* g-band (right panels) images of candidates A and B. Red stars mark the propagated *Gaia* positions at the *VHS* imaging epochs (2015 for A and 2013 for B), while yellow stars show the propagated *Gaia* positions at the RACS observation epoch (2021). Green plus signs (+) and crosses (×) mark the W3 and W4 centroids, respectively. The corresponding green W3 (solid) and W4 (dashed) high flux contours for candidates A and B are also shown, with all data measured in Section 3. The 1367.5 MHz radio source positions are indicated by blue crosses (×), with blue ellipses representing the 1367.5 MHz radio source size as determined by a PyBDSF fit. Blue plus signs (+) mark 1655.5 MHz radio-detected positions. In the *VHS* panels, red circles show stellar objects from the *VHS* catalogue. In the *Legacy* g-band panels, red circles indicate sources with PSF profiles, while red triangles mark REX sources using upward triangles and EXP sources using downward triangles. North (N) and east (E) directions are indicated by the compass marker in the bottom-right corner of the upper-left panel and apply to all cutouts. While the *WISE* emissions, the position of the candidate stars, and the radio source position for candidate A are spatially blended, candidate B exhibits alignment between the radio and *WISE* emissions, both of which are separated from the position of the star.

classifies this source as a likely galaxy with a 90% probability. We also validated this detection by inspecting the VMC K_s-band PSF residual, which confirmed the significance of the feature distinct from the stellar profile. (Figure 10). Crucially, while VMC J045603.25-741010.66 is 3.59″ away from the *Gaia* position of candidate star C, it is only 0.4″ from the *WISE* W3 centroid.

VMC J045603.25-741010.66, the companion source, lacks a significant counterpart in the *VMC* J and Y band images, as confirmed by both the *VMC* catalogue and our inspection of the corresponding image data. Furthermore, while the source remains faint in the *Legacy* DR10 r and i bands, it exhibits a detection of 3.6σ above the background in the *Legacy* z-band image.

4.4 Image diagnostics for candidate D, I and J

Candidates D, I, and J have complete Legacy imaging coverage but lack *VISTA* data; instead, they are covered by the *UKIRT* surveys. In the NIR regime, we analyse D and I using *UKIDSS* imaging data, and J using the *UHS*. Figure 11 presents the *Legacy* images used to assess the optical morphology of candidates D and I, while the *UKIDSS* images for them are shown in Figure 12.

For candidate D, the *Legacy* catalogue reveals a faint companion object. With an REX profile and the DESI Legacy ID 10995494344987809, this object is located in the south-east fringe of the stellar brightness profile. This object appears as a marginal detection in the r-band image (Figure 11), and is offset by 2.4″ from the W3 centroid position. For candidate I, the W3 centroid detected at low SNR appears to lie on the fringe of the stellar brightness profile, while the W4 centroid lies outside the profile. Despite the positional separation suggested by the *WISE* images, the *Legacy* catalogue did not identify any clear companion object located within 3″ of the position of the candidate star, unlike the case of candidate D. In the

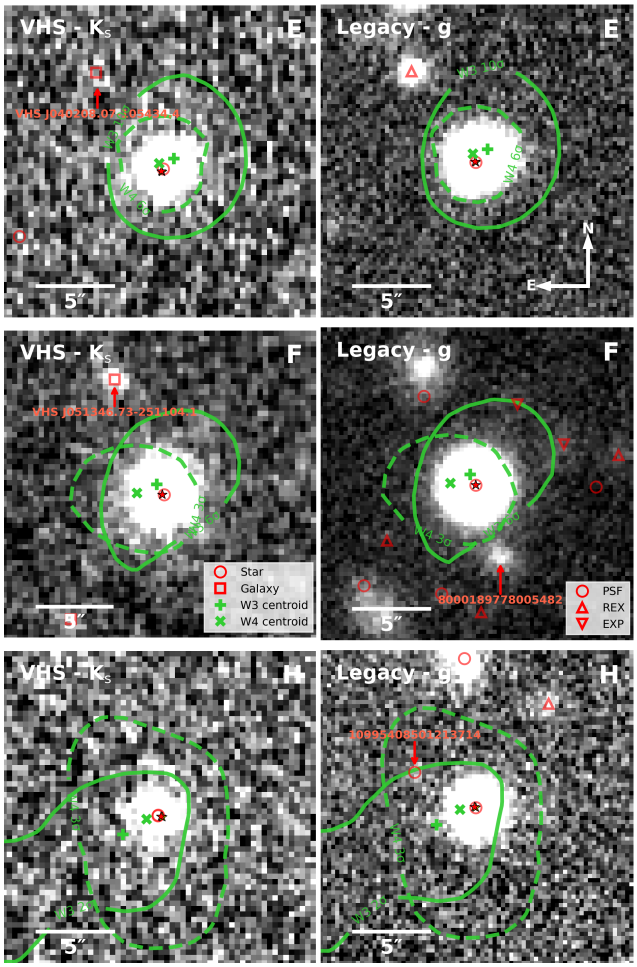

Figure 8. *VHS* K_s-band (left panels) and *Legacy* g-band (right panels) images of candidates E, F and H. Red stars mark the propagated *Gaia* positions at the *VHS* imaging epochs (2017 for E, 2016 for F, and 2012 for H), while yellow stars show the *Gaia* positions at the Gaia DR3 reference epoch (2016.0). Green plus signs (+) and crosses (×) mark the W3 and W4 centroids, respectively. The corresponding green W3 (solid) and W4 (dashed) high flux contours for candidates are also shown, with all data measured in Section 3. In the *VHS* panels, red circles show stellar objects from the *VHS* catalogue, and the red squares mark the galaxy-like objects. In the *Legacy* g-band panels, red circles indicate sources with PSF profiles, while red triangles mark REX sources using upward triangles and EXP sources using downward triangles. A compass in the upper-right panel (*Legacy* g-band) indicates the orientation for all subplots. Nearby companions are highlighted with red labels: VHS J040208.07−105434.4 in the K_s panel of candidate E; VHS J051346.73−251104.1 (K_s) and Legacy ID 8000189778005482 (g-band) for candidate F; and Legacy ID 10995408501213714 in the g-band panel of candidate H.

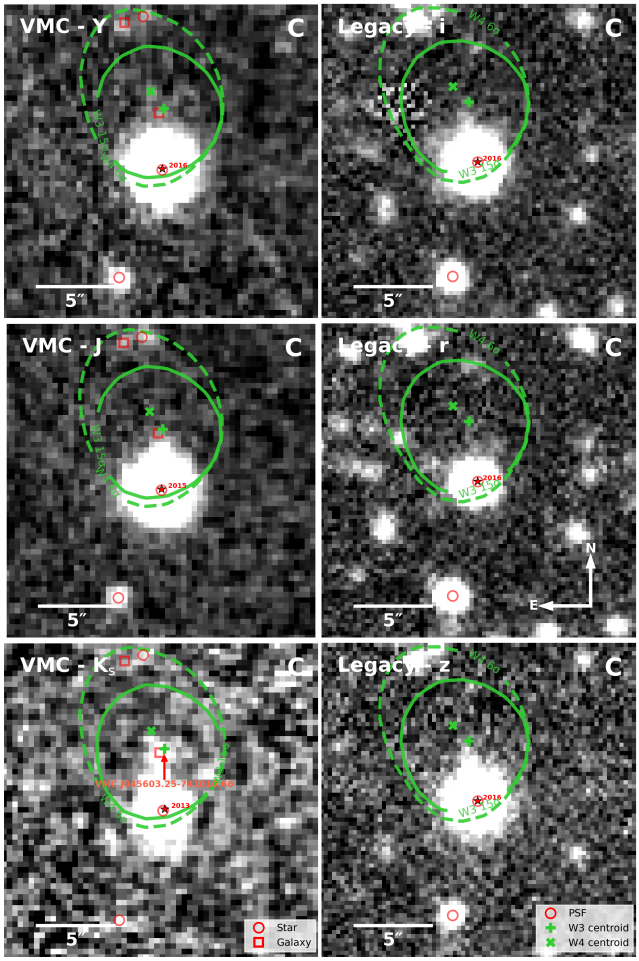

Figure 9. *VMC* Y, J, and K_s band (left panels) and *Legacy* DR10 i, r, and z band (right panels) images of candidate C. Red stars mark the stellar position at the respective imaging epochs: 2012.0 for the *VMC* images and 2016.0 (the *Gaia* DR3 epoch) for the *Legacy* images. Green plus signs (+) and crosses (×) mark the W3 and W4 centroids, respectively. The corresponding green W3 (solid) and W4 (dashed) high flux contours for candidates are also shown, with all data measured in Section 3. In the *VMC* panels, red circles denote stellar-like objects from the *VMC* catalogue, and the red squares mark the galaxy-like objects; in the *Legacy* panels, the red circles indicate sources best fit by PSF profiles. A compass in the middle-right panel (*Legacy* r-band) indicates the orientation for all subplots. VMC J045603.25-741010.66, highlighted by a red label, is visible north of the star, most significantly in the VMC K_s-band.

UKIDSS images (Figure 12), there are even fewer companion objects or nearby stars in the vicinity of the candidates D and I, and no case obviously indicates an explicit culprit.

In contrast, candidate J shows a blended morphology, with the *Legacy* image revealing a distinct bulge extending north-east from the stellar profile (Figure 13). This feature also behaves as a faint companion, located at the same position in the UHS NIR band images, most notably in the H band (Figure 14). However, this object is not catalogued as an independent source in either the *Legacy* or UHS catalogues. To evaluate its properties, we conducted photometric measurements across several optical and NIR bands. Figures 13 and 14 display the full-band Legacy and UHS maps, along with the residual maps of the vicinity after subtracting the stellar point spread function (PSF) of Candidate J. Table 11 presents the measurement results.

In the optical regime, this companion is most prominent in the g- and r-bands, where the photometric measurements are most reliable, yielding SNR = 14.8 and 13.4 respectively (Figure 13). The i-band image suffers from saturation and a bleed trail originating from candidate J, permitting only an unreliable measurement, while the source is faint and undetected above 3σ in the z band; these two bands are thus far less constraining than g and r. We attempt to fit the companion on the g- and r-band residuals and find that a PSF model

Table 11. Photometric extraction results of the optical/NIR companion source located 3″ away to candidate J, from *Legacy* DR10 ($griz$) and *UHS* (JHK) imaging.

Band	AB magnitude	Flux density F_ν (μJy)	Significance	Note
g	23.38 ± 0.07	1.61 ± 0.11	14.8σ	
r	22.42 ± 0.08	3.92 ± 0.29	13.4σ	
i	—	—	—	excluded (saturation / bleed trail)
z	> 23.27	< 11.27	< 3σ	~3.6σ residual peak
J	> 21.55	< 8.71	2.6σ	
H	21.05 ± 0.28	13.80 ± 3.56	3.9σ	tentative detection
K	> 20.74	< 18.37	0.3σ	

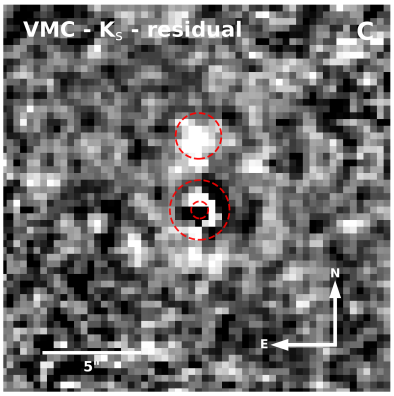

Figure 10. PSF residual images of candidate C in the VMC K_s band. The two central red dashed circles show the PSF FWHM and the 99% brightness profile of the stars. The offset red dashed circle marks VMC J045603.25-741010.66, the companion source detected outside the PSF brightness profile. North (N) and east (E) are indicated by the compass in the bottom-right corner.

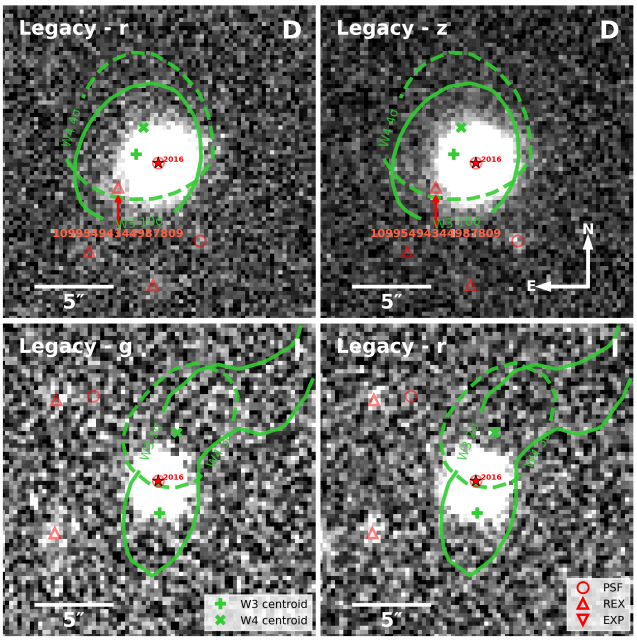

Figure 11. *Legacy* DR10 images for candidates D and I. The upper panels show the r-band and z-band images for candidate D, and the lower panels show the g-band and r-band images for candidate I. Each panel spans ~20″×20″ in RA and Dec. Red stars mark the *Gaia* positions at the *Gaia* DR3 epoch (2016.0). Green plus signs (+) and crosses (×) mark the W3 and W4 centroids, respectively. The corresponding green W3 (solid) and W4 (dashed) high flux contours for the candidates are also shown, with all data measured in Section 3. Red circles indicate sources with PSF profiles from the *Legacy* catalogue, red upward triangles mark REX sources, and red downward triangles mark EXP sources. North (N) and east (E) directions are indicated by the compass marker in the bottom-right corner of the upper-right panel and apply to all cutouts. One nearby companion, Legacy ID: 10995494344987809 for candidate D, is highlighted by annotation.

best describes its morphology, meaning the companion is consistent with a point source and cannot be spatially resolved at this resolution.

We also performed photometric extraction in the UHS NIR bands (Figure 14). The H band provides the best detection, recovering a 3.9σ source with an elongated, bar-like residual structure. In the J band, a nominal 2.6σ peak is present but is indistinct from the fringe features of the candidate star's brightness profile. In the K band, an elongated structure is again visible, but its significance is too low (SNR = 0.3) to make a convincing detection. Neither the J nor the K-band provides a clear detection comparable to that in H-band, or to the g and r-bands from the *Legacy* imaging.

This bulge-like companion lies ~ 3″ from both the W3 and W4 centroids. The Legacy DR10 also identified an EXP profile source (DESI Legacy ID 10995551421076405) ~ 5″ from candidate J, to the south-east of the W3 centroid. The complexity of the vicinity of candidate J, together with the results for the remaining candidates, is discussed and synthesised in Section 5.

5 DISCUSSION

5.1 Evaluating the Likelihood of Contamination for the Nine Candidates

Building on the multi-wavelength and astrometric diagnostics presented in Sections 3 and 4, we can now classify the nine Dyson Sphere star candidates based on the likelihood of extragalactic contamination. Similar to the analysis of candidate G, we integrate these archival findings to identify which sources show clear signs of background contaminants and which remain ambiguous.

5.1.1 *Candidates B and C: the most likely contaminated cases*

Candidates B and C represent the two cases exhibiting the strongest evidence of background contaminants contributing to the MIR excess. For these sources, the archival data reveal the presence of background objects consistent with the observed infrared anomalies. Compared to the control-sample M dwarfs of similar G-band magnitude and $W1/W2$ SNR, the two candidates exhibit significantly larger W1 and W2 bands emission centroid offsets from the propagated *Gaia* position, with a Gaussian-equivalent significance of > 2σ (Table 10).

As shown in Figures 3 and 7, the 1367.5 MHz and 1655.5 MHz radio sources of candidate B, along with the W3 and W4 centroids, are

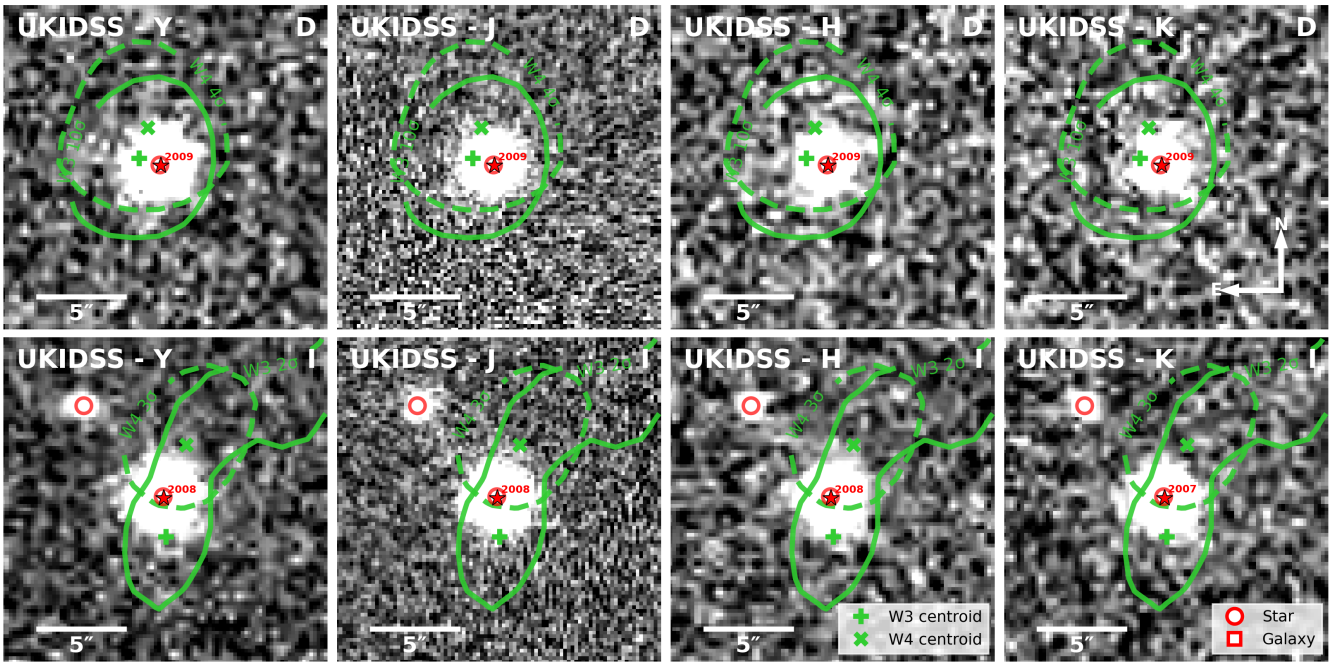

Figure 12. *UKIDSS YJHK* band images for candidates D and I, with each subplot displaying an 18″ × 18″ field of view. The upper panels display data for candidate D observed between August and October 2009, while the lower panels display data for candidate I observed between April 2007 and February 2008. Red stars mark the propagated *Gaia* positions at the precise observation epochs retrieved from the archive logs (annotated by year). Red circles indicate sources classified as stars within the companion survey catalogue. Green plus signs (+) and crosses (×) mark the W3 and W4 emission centroids, respectively. The corresponding green solid lines outline the W3 flux contours, and the green dashed lines outline the W4 contours. North (N) and east (E) directions are indicated by the compass marker in the bottom-right corner of the upper-right panel and apply to all cutouts.

all spatially associated with the faint, extended tail/bulge structure visible in the *Legacy Survey* images, lying at the fringe of Candidate B's PSF brightness profile. The spatial alignment, reinforced by the typical AGN radio spectral index of $\alpha \sim 0.59$ presented in Subsection 3.1, supports the presence of a background extragalactic source blended with the foreground candidate star B. The *WISE* emission maps (Figure 3) suggest that this background galaxy is likely a Hot DOG, which dominates the observed W3 and W4 bands MIR fluxes. From the view of *WISE*'s resolution, the 3″ galaxy-to-stellar offset makes the illusion that candidate star B itself is emitting the W3 and W4 excess fluxes, consistent with the predicted MIR signature of a modelled Dyson Sphere star.

Although candidate C lacks radio counterparts, its W3 and W4 emissions are offset from the central star by several arcseconds, similar to candidates B and G. The W3 and W4 centroids are spatially coincident with VMC J045603.25-741010.66, a source multiply detected in the *VMC* and *Legacy* surveys. Given that its location is nearly identical to the W3 centroid measured in our work, and there is no other nearby object detected, VMC J045603.25-741010.66 is likely the genuine contributor to the W3 and W4 band MIR flux excesses of candidate C. The *WISE* photometric characteristics of VMC J045603.25-741010.66 suggest that it is a potential hot DOG previously unknown to the literature. However, it appears undetected in both the RACS and GLEAM radio surveys. Frey et al. (2016). Such a non-detection is consistent with the typically radio-quiet nature of the Hot DOG population (Bridge et al. 2013). We further discuss the implications of this result and evaluate the expected radio-loud fraction of hot DOGs based on a sample of 144 confirmed hot DOGs in Section 5.2.

5.1.2 *Candidates A: a suggestive contaminated case*

Candidate A represents a highly suggestive case of contamination by a background Active Galactic Nucleus (AGN). Unlike candidates B and C, which have catalogued companions spatially separated from the position of the known star, candidate A's radio companion (RACS-DR1 J124512.7-265206) is blended with the star position and thus not distinct. The radio spectral index of RACS-DR1 J124512.7-265206 ($\alpha \sim 0.39$) is characteristic of a flat-spectrum AGN. The radio sources, WISE centroids, and the *Gaia* positions of the candidate stars are highly coincident, with mutual offsets of less than 2.5″. As shown in Figure 7, these positions align closely within the brightness profile of the candidate star, and archival optical/NIR imaging reveals no other nearby sources. Given the statistical rarity of a flat-spectrum radio source aligning so precisely with a foreground star, it is highly probable that the star's emission is being contaminated by a background AGN along the same line of sight. This alignment explains the minimal positional offsets observed across the different wavebands.

A further, independent line of evidence for this hidden AGN comes from the larger *AllWISE* centroid-to-stellar positional offsets compared to those of the control stars. In the Rayleigh significance analysis presented in Section 3.5, the offset between the Gaia position of candidate A and the *WISE* centroids yields the highest Gaussian-equivalent significance in both the W1 and W2 bands (Table 10), which offer the highest spatial resolution for characterising the stellar flux. That said, direct evidence is still lacking without dedicated high-resolution observations. Upcoming high-resolution observations from the JWST GO programme 7199 (Zackrisson et al.

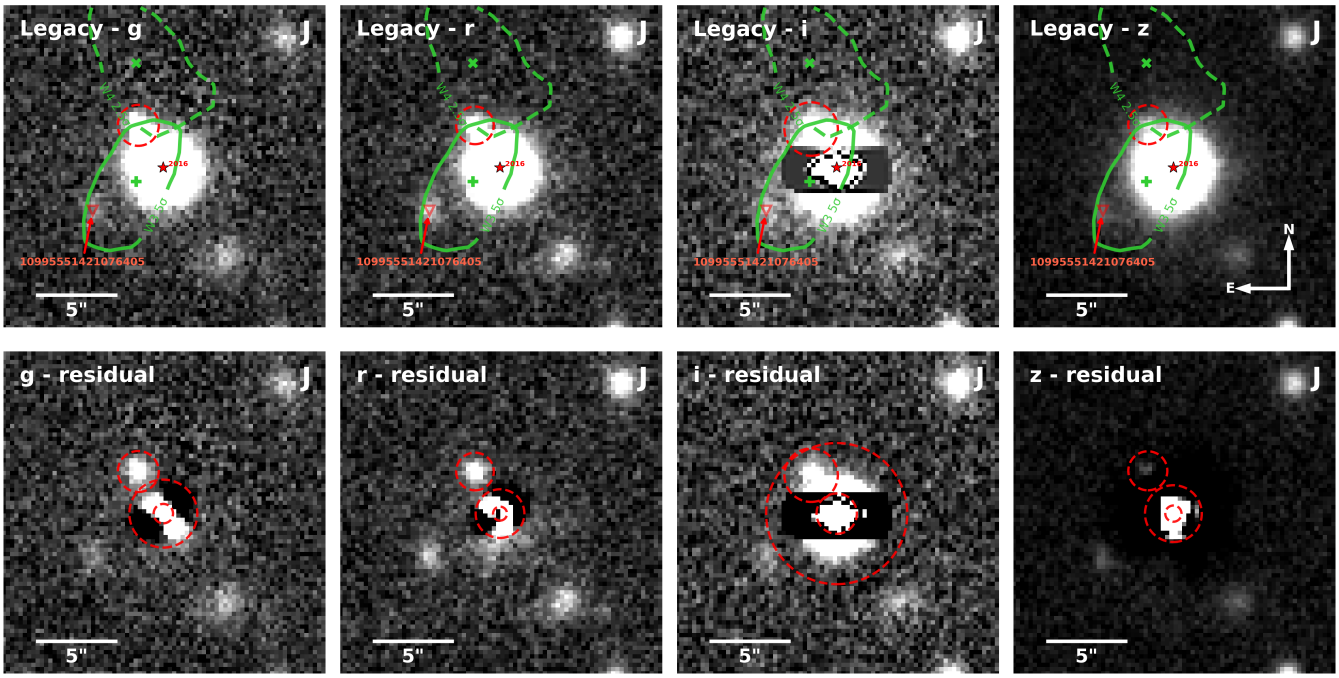

Figure 13. *Legacy* DR10 $griz$-band images (upper panels) and corresponding PSF-subtracted residual images (lower panels) for radio source candidate J, each displaying an 18″ × 18″ field of view. The upper panels show the original images, with standard WISE W3 emission centroids (green +) and W4 centroids (green ×) annotated. The solid green lines outline the W3 5σ flux contours, and the dashed green lines outline the W4 2.5σ contours. Red stars mark the Gaia stellar at the epoch of J2016.0. A nearby catalogued source (*Legacy* ID: 10995551421076405) is additionally highlighted by the red marker, label, and arrow in the upper panels. North (N) and east (E) directions are indicated by the compass marker in the bottom-right corner of the upper-right panel and apply to all cutouts. The lower panels display the residual images following subtraction of a fitted circular PSF model of candidate J. The two central red dashed circles show the PSF FWHM and the 99% brightness profile of candidate J, while the offset red dashed circle marks the position of the uncatalogued companion located ∼ 3″ to the north-west. The companion is recovered as a significant residual in the g and r-band images.

2025) using the MIRI instrument will be essential to disentangle the mid-infrared emission from the stellar profile.

5.1.3 *Candidates E, F, H and J: the candidates with ambiguous evidence*

Candidates E and F present more ambiguous evidence than candidates A, B, and C, as they exhibit lower MIR centroid-to-stellar offsets and have no detected companion objects near the stellar brightness profile fringe that resemble extragalactic sources. While candidates A, B, and C exhibit W3 offsets exceeding 2″, they also show Gaussian-equivalent significances of at least 2σ in both W1 and W2, derived from fitting a Rayleigh distribution to the control-star centroid offsets. By contrast, candidates E and F display > 2σ significance in only a single W1 or W2 band (Table 10), and their W3 offsets are also smaller. Specifically, candidate E shows a ∼ 3.3σ significance in the W1 band under a Rayleigh distribution scale (rather than a median scale), whereas candidate F exhibits a 2.7σ significance in the W2 band under the median scale. The W3 offsets for both candidates E and F remain below 1.5″ (Table 5).

The inspection of the images in Subsection 4.2 provides supplementary evaluation for candidates E and F. For candidate E, the closest external object is a galaxy-like source (VHS J040208.07-105434.4) located > 5″ away, which is too distant to interfere with the stellar MIR flux (Figure 8). Similarly, for candidate F, the nearest catalogued source—a PSF-profile object in the Legacy DR10 Tractor—is located over 5″ to the north. Additional faint objects near candidate F, including a southern EXP-profile source (Legacy DR8 ID: 8000189778005482) and several northeastern sources, also lie well outside the main MIR emission region.

Given that the visible neighbouring sources identified for candidates E and F are situated too distant to plausibly influence the MIR photometry, the > 2σ Gaussian-equivalent centroid offsets significance, which appear in the W2 band for E, and the W1 band for F, serve as indirect evidence of background contamination. The W1 and W2 bands are capable of tracing the stellar photosphere with high precision; therefore, significant offsets in these bands provide a reliable indicator of an underlying, unresolved source, even if the W3 flux is expected to be more strongly dominated by emission from a putative interloper. Although the overall evidence strength for E and F is lower than that of A, B, and C, the lack of spatially coincident background sources in deep survey imaging and photometric data suggests that while contaminants for E and F are likely present, the sources must be highly blended with the target stars.

Candidate H represents another ambiguous case. Its W3-band centroid is offset by ∼ 3.5″ from the *Gaia* position of the star and exceeds the W3-band offsets of candidates B and C. This is the highest W3-band offset and the only one exceeding 3″ among all nine candidates throughout this paper, while its W1 and W2 band offsets are only ∼ 0.5″. Although the quantitative Rayleigh test in Subsection 3.5 suggests that the W3 offset does not deviate significantly from the control star distribution, the control sample contains only five stars. Therefore, this statistical result should not obscure the reality of the high positional W3-band offset of candidate H, which is clearly visi-

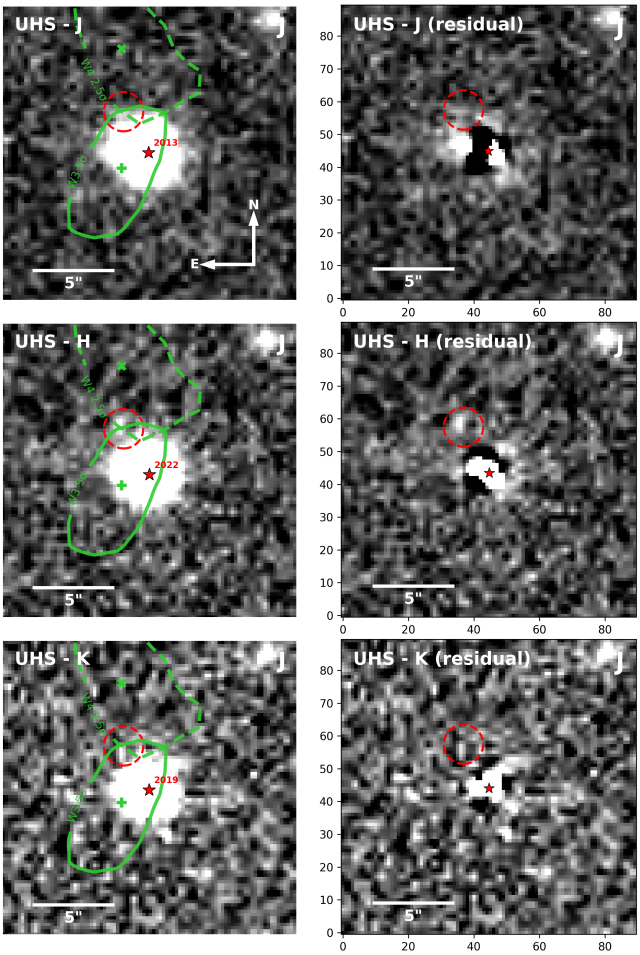

Figure 14. *UHS DR2* NIR data and corresponding PSF-subtracted residual images for radio source candidate J across the J, H, and K bands, each displaying an $18'' \times 18''$ field of view. The left panels show the original multi-band stacked images, with standard WISE W3 emission centroids (green +) and W4 centroids (green ×) mapped. The solid green lines outline the W3 3σ flux contours, while the dashed green lines outline the W4 2.5σ contours. Red stars mark the Gaia positions propagated via proper motions to the per-band observation epoch (annotated by year: 2013, 2022, 2019). North (N) and east (E) directions are indicated by the compass marker in the bottom-right corner of the upper-left panel and apply to all cutouts. The right panels display the residual images following subtraction of a fitted circular PSF model, revealing persistent, non-stellar near-infrared emission coincident with the pre-computed W4 centroid location, as highlighted by the red dashed circle.

ble in Figure 5. Although its W4 centroid offset is smaller ($< 2.5''$), the spatial MIR emission morphology appears elongated.

Using *Legacy* Survey data, we identified a faint object with a PSF brightness profile—likely a background galaxy (LegacyID: 10995408501213714)—situated to the northeast of candidate star H that contributes to the W4 flux (Figure 8). The blending of these two sources may result in the observed elongation of the W4 emission region. However, the SNR for the W3 and W4 emissions of candidate H is low ($\sim 3\sigma$), significantly undermining the reliability of its measured offsets. Furthermore, unlike candidate C, where the catalogued background galaxy is nearly coincident with the W3-band centroid, the catalogued background galaxy near candidate H lies $\sim 3''$ from the W3 centroid.

The final ambiguous case is candidate J. As detailed in Section 4.4, we retrieved photometric evidence for an uncatalogued companion source at the stellar fringe, detected consistently in the *Legacy* g and r bands and tentatively in the UHS H band, and exhibiting a point-source morphology. This companion is not, however, the only source projected onto the W3 emission of candidate J: it lies $3.35''$ from the W3 centroid and $3.94''$ from the W4 centroid, while the *Legacy* DR10 Tractor catalogue separately lists a resolved, galaxy-like source with an exponential (EXP) profile (*Legacy* ID 10995551421076405; Figure 13). As with candidate H, both putative contributors to the MIR flux are offset from the W3 centroid by $\sim 3''$ rather than being coincident with it.

Since the candidate star J, the companion, and the catalogued galaxy-like source (*Legacy* ID: 10995551421076405) all lie within the W3 $> 5\sigma$ emission region, the W3 flux cannot be unwarrantably attributed to a single source: owing to the blending and co-location within the *WISE* beam, it may plausibly be dominated by the star, by the companion, by the galaxy-like source, or by a combination of these objects. The W4 emission, by contrast, exhibits a significant positional offset from both the candidate star and the catalogued galaxy-like source, leaving the companion as the only optical/NIR feature that could be preliminarily identified as a contributor to the W4 flux. We accordingly regard candidate J as an ambiguous case of background contamination; unlike candidates A and B, whose blended companion can be identified as an AGN through its radio spectral index, the companion of candidate J lacks comparably direct evidence for its nature, and definitively assigning the mid-infrared emission to any single feature will require future observations of higher angular resolution and sensitivity. Given the lack of exact spatial coincidence between the identified galaxies and the W3 centroids, both candidates H and J carry significantly lower confidence than candidates A, B and C. Consequently, we relegate both candidates H and J to a lower, ambiguous classification tier.

In summary, while the specific evidence for candidates E, F, H, and J is more ambiguous than for A, B, and C, owing variously to low SNR, blending, or the lack of spatially coincident background sources, their significant positional offsets still indicatively suggest background contamination. Resolving these cases requires dedicated higher-resolution observations, such as the approved observations of candidate E via the JWST GO programme 7199 (Zackrisson et al. 2025).

5.1.4 Candidates that lack critical evidence for MIR contamination

Candidates D and I lack both clear evidence of contamination and the definitive proof needed for a final classification. Without radio detections, their analysis relies solely on *ALLWISE* centroids and archival optical/NIR imaging analysis, following the same methodology used for candidates C, E, F, H, and J.

Candidate D presents a spatial contradiction: while *Legacy* imaging reveals an REX-profile galaxy (*Legacy* ID: 10995494344987809) on the southeastern fringe of the stellar profile (Figure 11), the *WISE* centroids are oriented toward the north. The MIR imaging shows no clear spatial separation between the WISE MIR spatial emission and the position of candidate star D (Figure 4). As detailed in Subsection 3.4, candidate D exhibits the smallest positional offset among all the candidates. Furthermore, the four-band comparison with the control star offsets presented in Subsection 3.5 demonstrates that none of the *WISE* bands for candidate D pass the Rayleigh distribution test, suggesting that its offsets are statistically indistinguishable from the control population. A plausible explanation for the low-level excess is a proximate, highly blended AGN—an arrangement analogous to the blending of candidate A, but without radio emission to confirm an

extragalactic nature. Despite candidate D lying within the footprint of multiple major radio surveys ($\delta \approx +05°$), the absence of a radio counterpart suggests that any contaminant would have to be radio-quiet. Ultimately, the true origin of this emission will be determined by high-resolution MIRI data from the *JWST* GO 7199 programme (Zackrisson et al. 2025).

The final case is candidate I. Its W3 centroid appears to be located on the fringe of the stellar brightness profile, while the W4 centroid is positioned outside the profile. The W3 emission, however, displays a stripe-like structure with only $\sim 2\sigma$ significance, making it ambiguous for reliably indicating the true background source position. Its W4 emission, with $> 3\sigma$ significance, shows an offset of $\sim 3.2''$ from the *Gaia* position of the star. However, the comparison in Subsection 3.5 does not support the presence of a significant offset discrepancy relative to the control stars. Unlike candidates H and J, for which deep optical/NIR imaging revealed sources projected onto the high W3 and/or W4 flux regions, we find no such counterpart for the MIR emission of candidate I in the deep *Legacy* Survey and *UHS* images. Candidate I has neither a statistically robust positional offset, unlike candidates E and F, nor an identifiable optical/NIR counterpart, unlike candidates H and J. It therefore presents the weakest evidence among the candidates. We accordingly place it in the lowest classification class, along with candidate D. If a faint background AGN spatially coincident with the stellar profile is the genuine MIR contributor, high-resolution imaging will be required to disentangle these components, particularly since candidate I was not included in the *JWST* GO 7199 programme.

Finally, all the potential hot DOG contaminants analysed in Subsection 5.1 are presented in Table 12.

5.2 The Radio Detection Rate of Hot Dust-Obscured Galaxies

Among the ten Dyson Sphere candidates analysed in this work, only three (A, B, and G) were detected in archival radio surveys. If one assumes that all ten candidates are contaminated by Hot Dust-Obscured Galaxies (Hot DOGs), the remaining seven would necessarily be radio-quiet AGNs. To evaluate the plausibility of this scenario, we examined a sample of 144 catalogued Hot DOGs from Assef et al. (2015)—a robust sample selected from *WISE* data and verified with ground-based NIR observations.

We queried the VizieR service for radio counterparts within this reference sample and identified only 12 detections (Table 13), representing a detection rate of $< 10\%$. The radio catalogues include: the FIRST survey(Becker et al. 1995), NVSS (Condon et al. 1998), SUMSS (Mauch et al. 2003), the TIFR GMRT Sky Survey (TGSS; Intema et al. 2017), the Australia Telescope Compact Array XXL survey (ATCA XXL; Butler et al. 2018), the VLA Sky Survey (VLASS; Lacy et al. 2020), the RACS surveys (Hale et al. 2021; Duchesne et al. 2024, 2025), the LOFAR Two-metre Sky Survey Data Release 2 (LoTSS DR2; Shimwell et al. 2022), and the GLEAM-X survey (Ross et al. 2024). This low detection rate is consistent with the characterisation of similar WISE-selected dusty extragalactic sources as typically radio-quiet (Bridge et al. 2013). Consequently, the lack of radio emission in seven out of ten candidates aligns with the low radio-loud fraction expected for this galaxy class.

6 CONCLUSIONS

We conducted a combined analysis of nine Project Hephaistos Dyson Sphere candidates using two complementary approaches based on archival data: (1) an astrometric examination of AllWISE four-band image centroids to identify mid-infrared (MIR) flux offsets relative to the *Gaia* positions propagated to the *ALLWISE* epoch, a method whose effectiveness can be validated through a comparative analysis of ordinary M-dwarf control samples, and (2) a search for potential extragalactic companions in deep NIR and optical images.

By comparing the WISE centroids with the Gaia stellar positions (the first method), we found that candidates B and C exhibit the largest positional offsets, with W3 centroid-to-stellar offsets of approximately $3''$. Notably, the W3 centroid of candidate B aligns with RACS 1367.5 MHz and 1655.5 MHz radio counterparts to within $< 1''$, indicating that a radio source dominates the emission observed in the W3 and W4 bands.

Using the second method—searching for extragalactic companions in deep imaging, we confirmed that J2335-0004, the Hot DOG which contaminated candidate G, is present and catalogued in the VISTA and Legacy surveys. Although no radio companion was found near candidate C, we found a faint NIR source located at the position of the W3 centroid in the VMC data. These results suggest that both B and C are likely Hot DOGs, similar to the MIR positional offset observed in candidate G, which was later confirmed as a hot DOG by high-resolution radio observations (Ren, Garrett & Siemion 2025).

We also identified candidate A as a suggestive case. It exhibits a radio counterpart with an AGN-like spectral index. Because its centroid-to-stellar offset is far larger than those of the control sample stars, the close proximity between the *Gaia* positions of the star, radio source, and WISE centroids implies that the contaminating background source must lie nearly along the line of sight.

Candidates E, F, H and J are classified as a lower, ambiguous class: marginal cases requiring further evidence to assess the potential contamination. For E and F, although their MIR centroid-to-stellar offsets reach a Gaussian-equivalent significance above 2σ in one of the four WISE bands, the remaining bands show no offset excess, and no counterparts can be confirmed in deep imaging to serve as a clear source of contamination. Candidate H displays the largest W3-band offset among the nine candidates, and candidate J exhibits multiple likely background contaminants; for both, some possible contaminating sources were identified nearby, but low SNR or blending limits the reliability of these associations.

Lastly, candidates D and I show no radio counterparts, no unambiguously outstanding centroid offsets, and no faint companions that could plausibly contribute to the MIR excess. However, we suspect that these sources might also be contaminated by radio-quiet AGNs that lie close to the line of sight towards the M-dwarf star. Our identification of a sample of 144 Hot DOGs suggests that more than 90% of them are radio-quiet. This result agrees with the low radio-detection rate observed in the Project Hephaistos Dyson Sphere candidate sample.

Despite the resolution limitations of current MIR datasets like the WISE archive, our analysis demonstrates that supplementary multi-wavelength data offer valuable insights into the nature of these Dyson Sphere candidates. The suspected contaminants near Candidates B and C still require confirmation of their extragalactic nature. Dedicated observations, such as deep infrared imaging and spectral analysis, are essential to conclusively disentangle hypothetical Hot DOGs from the foreground stars. Such observations are equally critical for resolving the possible cases (A, E, F, H, and J) and clarifying the nature of candidates D and I, where radio data remains insufficient. In this regard, the ongoing JWST GO 7199 observations of Candidates A, D, and E will provide the direct results needed to identify the genuine contributors to their infrared excess. Ultimately, rigorously identifying and eliminating such false positives is a fundamental step in the search for techno-signatures; by systematically ruling out nat-

Table 12. Summary of potential background contaminants among the Dyson Sphere candidates.

Candidate	Evidence Strength	Likely Contaminant ID	Note
A	Suggestive	RACS-DR1 J124512.7-265206	Exhibits AGN-like radio spectrum
B	Strong	RACS-DR1 J035603.8-403148	Exhibits AGN-like radio spectrum
C	Strong	VMC J045603.25-741010.66	
D	Weak	–	
E	Ambiguous	–	
F	Ambiguous	–	
H	Ambiguous	Legacy 10995408501213714	
I	Weak	–	
J	Ambiguous	Legacy 10995551421076405	An uncatalogued companion source identified

Table 13. Radio detections for the sample of 144 catalogued Hot DOGs.

WISE ID	Survey	Central Frequency	Flux Density (mJy)
J022052.12+013711.6	VLA[a]	6.2 GHz	0.20 ± 0.01
J022646.85+051422.7	NVSS	1.4 GHz	6.10 ± 0.50
	FIRST	1.4 GHz	6.49 ± 0.12
	VLASS	3.0 GHz	3.22 ± 0.23
J075725.07+511319.7	FIRST	1.4 GHz	3.57 ± 0.15
	NVSS	1.4 GHz	3.20 ± 0.50
J085124.78+314856.1	LoTSS DR2	144 MHz	5.22 ± 2.83
J094608.30+500820.4	LoTSS DR2	144 MHz	6.64 ± 1.16
	FIRST	1.4 GHz	1.21 ± 0.16
J100636.34+510500.7	LoTSS DR2	144 MHz	31.95 ± 9.64
	TGSS	147 MHz	40.0 ± 9.0
	FIRST	1.4 GHz	4.13 ± 0.13
	NVSS	1.4 GHz	3.20 ± 0.40
	VLASS	3.0 GHz	2.02 ± 0.25
J114612.87+412914.4	LoTSS DR2	144 MHz	4.38 ± 1.89
	FIRST	1.4 GHz	4.39 ± 0.13
	NVSS	1.4 GHz	4.10 ± 0.40
	VLASS	3.0 GHz	2.39 ± 0.20
J145705.92+293231.6	LoTSS DR2	144 MHz	2.10 ± 1.67
J154840.15+263029.3	RACS-low	850 MHz	2.27 ± 0.46
	RACS-mid	1367.5 MHz	1.97 ± 0.41
	FIRST	1.4 GHz	0.96 ± 0.14
J160357.39+274553.2	RACS-low	850 MHz	3.75 ± 0.66
	RACS-mid	1367.5 MHz	2.10 ± 0.50
	FIRST	1.4 GHz	2.28 ± 0.14
	NVSS	1.4 GHz	2.80 ± 0.50
	RACS-high	1655.5 MHz	1.68 ± 0.39
	VLASS	3.0 GHz	0.86 ± 0.17
J171400.14+524231.6	FIRST	1.4 GHz	2.76 ± 0.13
	NVSS	1.4 GHz	2.80 ± 0.40
	VLASS	3.0 GHz	1.30 ± 0.25
J233953.74-561301.1	GLEAM	200 MHz	86 ± 0.50
	SUMSS	843 MHz	21.2 ± 1.1
	RACS-low	850 MHz	17.84 ± 0.40
	RACS-mid	1367.5 MHz	11.28 ± 0.81
	RACS-high	1655.5 MHz	9.05 ± 0.97
	ATCA XXL	2.1 GHz	7.70 ± 0.39

[a] Hwang et al. (2018).

ural contamination, we can ensure that future resources focus only on the most robust and compelling Dyson Sphere candidates.

ACKNOWLEDGEMENTS

We sincerely thank the referee for the helpful suggestions, which have significantly improved the manuscript. TR and MAG applied the centroid analysis originally developed for their Candidate G investigation. EZ first noted the faint, fuzzy feature near Candidate C, motivating the development of the deep-image inspection method used in this study. AB was supported by the SNSA. TR is funded by the China Scholarship Council.

DATA AVAILABILITY

This work used software: Astroquery (Ginsburg et al. 2019), Astropy(Astropy Collaboration et al. 2013, 2018, 2022), NumPy (Harris et al. 2020), Photutils (Bradley et al. 2024), Matplotlib (Hunter 2007), SEP (Barbary 2016), SciPy (Virtanen et al. 2020). This work used data from the Aladin Sky Atlas (Bonnarel et al. 2000), AllWISE (Cutri et al. 2021; WISE Team 2020), the Australia Telescope Compact Array XXL survey (ATCA XXL; Butler et al. 2018), the Dark Energy Survey (DES; Dark Energy Survey Collaboration et al. 2016; DES DR1: Abbott et al. 2018; DES DR2: Abbott et al. 2021), the DESI Legacy Imaging Surveys (Dey et al. 2019), ESASky (Baines et al. 2017; Giordano et al. 2018), the FIRST survey (Becker et al. 1995), *Gaia* (Gaia Collaboration et al. 2016, 2023), the GLEAM-X survey (Ross et al. 2024), HEASARC, the LOFAR Two-metre Sky Survey Data Release 2 (LoTSS DR2; Shimwell et al. 2022), NVSS (Condon et al. 1998), the Panoramic Survey Telescope and Rapid Response System (Pan-STARRS; Chambers et al. 2016), the RACS surveys (Hale et al. 2021; Duchesne et al. 2024, 2025), Simbad (Wenger et al. 2000), SkyMapper (Onken et al. 2024), SUMSS (Mauch et al. 2003), the TIFR GMRT Sky Survey (TGSS; Intema et al. 2017), the Two Micron All Sky Survey (2MASS) (Skrutskie et al. 2006), the Very Large Array Sky Survey (VLASS; Lacy et al. 2020), and the VISTA Science Archive (Cross et al. 2012). The data supporting this article will be made available by the corresponding author upon reasonable request.

REFERENCES

Abbott T. M. C., et al., 2018, ApJS, 239, 18
Abbott T. M. C., et al., 2021, ApJS, 255, 20
Assef R. J., et al., 2015, ApJ, 804, 27
Astropy Collaboration et al., 2013, A&A, 558, A33
Astropy Collaboration et al., 2018, AJ, 156, 123
Astropy Collaboration et al., 2022, ApJ, 935, 167
Baines D., et al., 2017, PASP, 129, 028001
Barbary K., 2016, Journal of Open Source Software, 1, 58
Becker R. H., White R. L., Helfand D. J., 1995, ApJ, 450, 559
Bertin E., Arnouts S., 1996, A&AS, 117, 393
Blain A. W., 2024, arXiv e-prints, p. arXiv:2409.11447
Bonnarel F., et al., 2000, A&AS, 143, 33
Bradley L., et al., 2024, astropy/photutils: 1.13.0, doi:10.5281/zenodo.12585239, https://doi.org/10.5281/zenodo.12585239
Bridge C. R., et al., 2013, ApJ, 769, 91
Butler A., et al., 2018, A&A, 620, A16
Chambers K. C., et al., 2016, arXiv e-prints, p. arXiv:1612.05560
Cioni M.-R. L., et al., 2011, A&A, 527, A116
Condon J. J., Cotton W. D., Greisen E. W., Yin Q. F., Perley R. A., Taylor G. B., Broderick J. J., 1998, AJ, 115, 1693
Cross N. J. G., et al., 2012, A&A, 548, A119

Cutri R. M., et al., 2021, VizieR Online Data Catalog: AllWISE Data Release (Cutri+ 2013), VizieR On-line Data Catalog: II/328. Originally published in: IPAC/Caltech (2013)
Dark Energy Survey Collaboration et al., 2016, MNRAS, 460, 1270
Dey A., et al., 2019, AJ, 157, 168
Duchesne S. W., et al., 2024, Publ. Astron. Soc. Australia, 41, e003
Duchesne S. W., et al., 2025, Publ. Astron. Soc. Australia, 42, e038
Dye S., et al., 2018, MNRAS, 473, 5113
Dyson F. J., 1960, Science, 131, 1667
Fabricius C., et al., 2016, A&A, 595, A3
Frey S., Paragi Z., Gabányi K. É., An T., 2016, MNRAS, 455, 2058
Gaia Collaboration et al., 2016, A&A, 595, A1
Gaia Collaboration et al., 2023, A&A, 674, A1
Garrett M. A., Siemion A. P. V., 2023, MNRAS, 519, 4581
Ginsburg A., et al., 2019, AJ, 157, 98
Giordano F., et al., 2018, Astronomy and Computing, 24, 97
Hale C. L., et al., 2021, Publ. Astron. Soc. Australia, 38, e058
Hambly N. C., et al., 2008, MNRAS, 384, 637
Harris C. R., et al., 2020, Nature, 585, 357
Howell S. B., 2006, Handbook of CCD Astronomy. Cambridge Observing Handbooks for Research Astronomers Vol. 5, Cambridge University Press
Hunter J. D., 2007, Computing in Science and Engineering, 9, 90
Hwang H.-C., Zakamska N. L., Alexandroff R. M., Hamann F., Greene J. E., Perrotta S., Richards G. T., 2018, MNRAS, 477, 830
Intema H. T., Jagannathan P., Mooley K. P., Frail D. A., 2017, A&A, 598, A78
Korn A. J., Suazo M., Zackrisson E., Cortés-Zuleta P., Rains A. D., Nabizadeh A., 2026, arXiv e-prints, p. arXiv:2607.25701
Lacy M., et al., 2020, PASP, 132, 035001
Lane W. M., Cotton W. D., van Velzen S., Clarke T. E., Kassim N. E., Helmboldt J. F., Lazio T. J. W., Cohen A. S., 2014, MNRAS, 440, 327
Lawrence A., et al., 2007, MNRAS, 379, 1599
Mauch T., Murphy T., Buttery H. J., Curran J., Hunstead R. W., Piestrzynski B., Robertson J. G., Sadler E. M., 2003, MNRAS, 342, 1117
McMahon R. G., Banerji M., Gonzalez E., Koposov S. E., Bejar V. J., Lodieu N., Rebolo R., VHS Collaboration 2013, The Messenger, 154, 35
Miville-Deschênes M.-A., Lagache G., 2005, ApJS, 157, 302
Montalto M., et al., 2021, A&A, 653, A98
Ochsenbein F., Bauer P., Marcout J., 2000, A&AS, 143, 23
Onken C. A., Wolf C., Bessell M. S., Chang S.-W., Luvaul L. C., Tonry J. L., White M. C., Da Costa G. S., 2024, Publ. Astron. Soc. Australia, 41, e061
Ren T., Garrett M. A., Siemion A. P. V., 2024, Research Notes of the American Astronomical Society, 8, 145
Ren T., Garrett M. A., Siemion A. P. V., 2025, MNRAS, 538, L56
Ross K., et al., 2024, Publ. Astron. Soc. Australia, 41, e054
Shimwell T. W., et al., 2022, A&A, 659, A1
Skrutskie M. F., et al., 2006, AJ, 131, 1163
Suazo M., 2024, PhD thesis, Uppsala University, Uppsala, `http://urn.kb.se/resolve?urn=urn:nbn:se:uu:diva-524893`
Suazo M., Zackrisson E., Wright J. T., Korn A. J., Huston M., 2022, MNRAS, 512, 2988
Suazo M., Zackrisson E., Mahto P. K., Lundell F., Nettelblad C., Korn A. J., Wright J. T., Majumdar S., 2024, MNRAS, 531, 695
Theissen C. A., West A. A., 2017, AJ, 153, 165
Tsai C.-W., et al., 2015, ApJ, 805, 90
Virtanen P., et al., 2020, Nature Methods, 17, 261
WISE Team 2020, AllWISE Atlas (L3a) Coadd Images, NASA IPAC DataSet, IRSA153, doi:10.26131/IRSA153
Weiler M., 2018, A&A, 617, A138
Wenger M., et al., 2000, A&AS, 143, 9
Wright J. T., 2020, Serbian Astronomical Journal, 200, 1
Wright E. L., et al., 2010, AJ, 140, 1868
Zackrisson E., et al., 2025, Anomalous infrared fluxes of M dwarfs, JWST Proposal. Cycle 4, ID. #7199

APPENDIX A: CENTROID-OFFSET DISTRIBUTIONS OF THE CONTROL SAMPLES

As described in Section 3.5, we performed the centroid analysis on the full set of 155 control stars, grouped into nine control samples corresponding to the nine candidates. To illustrate the procedure, Figure A1 shows the centroiding results for the 15 control stars of Candidate A as an example. For each star and WISE band, we mark the *Gaia* position propagated to the corresponding WISE observation epoch and the measured centroid, from which the positional offset and associated uncertainty are derived. During the positional analysis of the control stars, the *Gaia* astrometric data are used to propagate the stellar positions to the WISE observation epochs, accounting for proper motion and parallax.

To further address the centroiding analysis presented in Section 3.5, we provide the complete set of results for all targets in Fig. A2. This figure displays the full grid of centroid-offset distributions for the control samples of nine candidates across the four WISE bands. In each panel, a direct visual comparison can be made between the distribution of the background control stars and the specific offset of the candidate. This comprehensive visualisation directly reflects the statistical metrics compiled in Table 10; in particular, the significantly higher offsets of candidates A, B, C, E, and F relative to their baseline control populations are clearly apparent.

This paper has been typeset from a TEX/LATEX file prepared by the author.

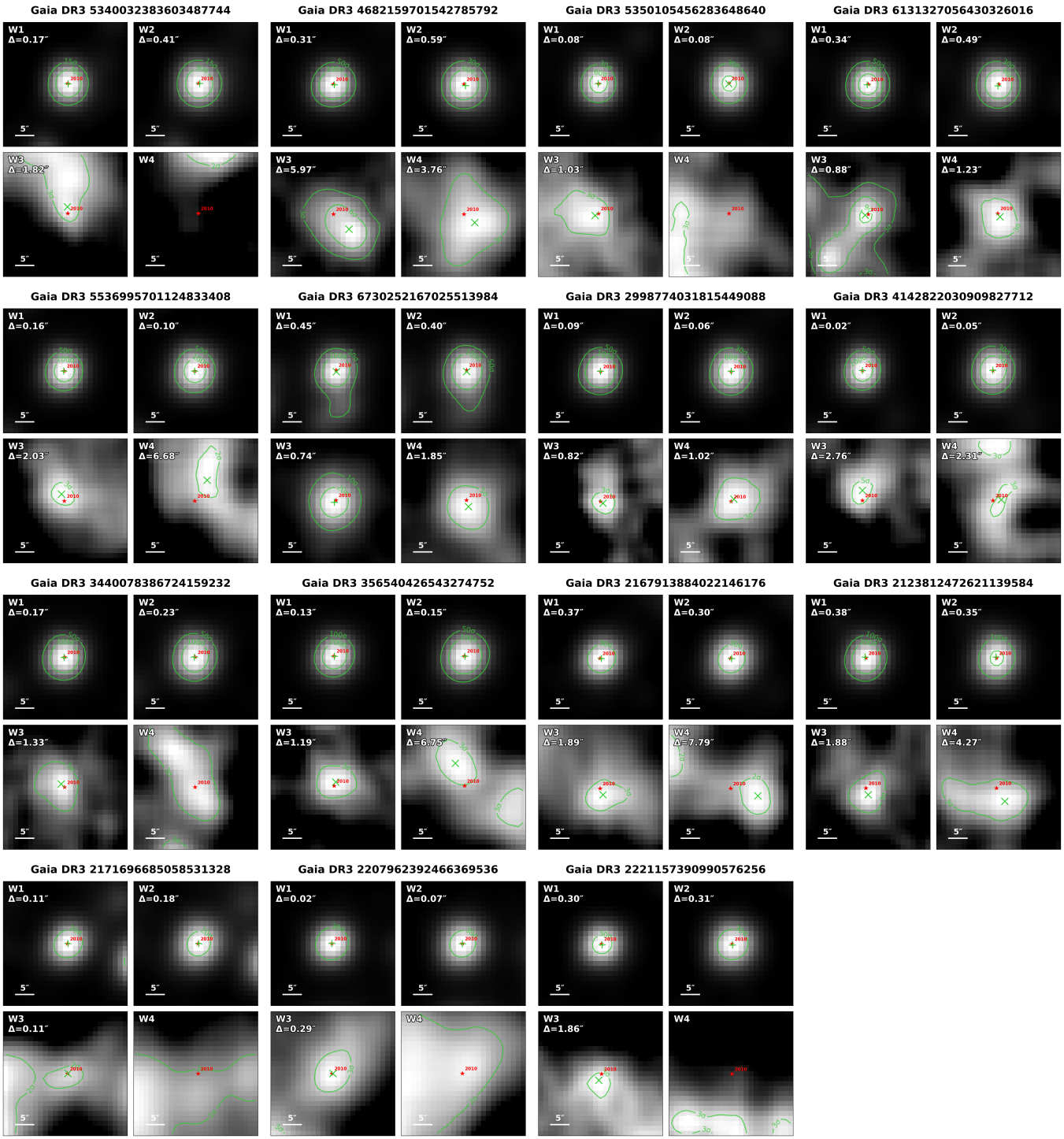

Figure A1. *ALLWISE* infrared images of the 15 control-sample stars for candidate star A. For each star, the four WISE bands are shown, each panel spanning a field of view of 30″ × 30″. Green contours show surface brightness at multiple σ levels above the background, where σ is the per-pixel background noise (RMS), and the green crosses (×) and plus signs (+) mark the MIR centroids. The red star indicates the propagated *Gaia* position at the *AllWISE* epoch. The angular offset, Δ, between the propagated *Gaia* position and the measured centroid is labelled in each panel. Note that three candidate stars lacked significant W4 emission and were consequently excluded from the W4 centroid fitting.

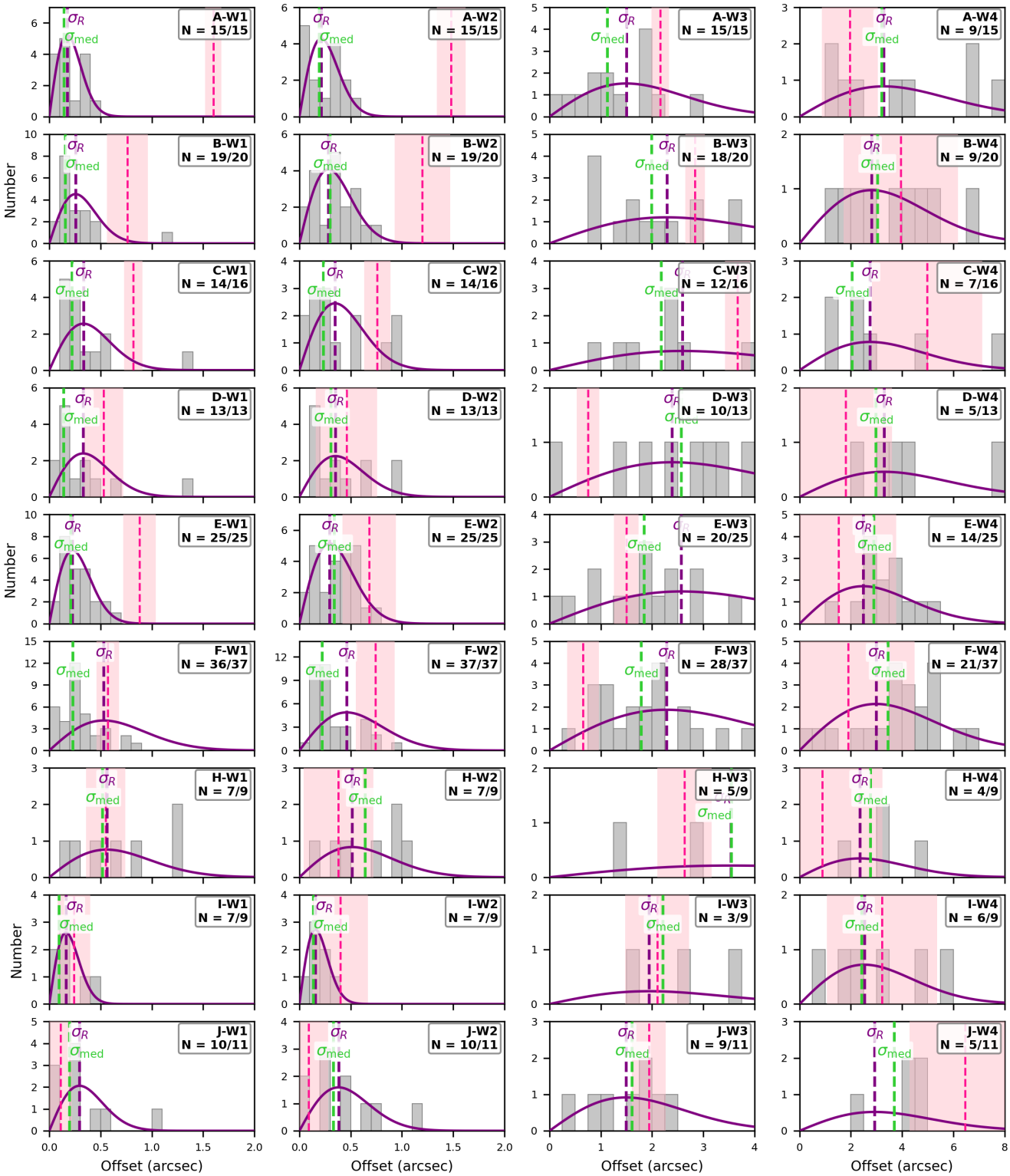

Figure A2. Distributions of *AllWISE* centroid-to-stellar-position offsets for the control-star samples of the candidates A, B, C, D, E, F, H, I and J, with one candidate per row and the four WISE bands across the columns. In each panel the grey histogram shows the number of control stars per offset bin, with bin widths of 0.1 ″ for W1 and W2, 0.25 ″ for W3, and 0.5 ″ for W4. The solid purple curves display the maximum-likelihood Rayleigh distribution fitted to that control sample; the purple dashed lines mark its Rayleigh scale parameter σ_R, and the limegreen dashed lines show the median-based robust scale $\sigma_{\rm med}$. The light-red shaded band gives the measured offset of the corresponding candidate star, its half-width the 1σ centroid uncertainty, and the red dashed line marks the central value. The number of control stars with successful centroid fits is given in each panel as $N = n/n_{\rm tot}$.